AD-A272 123

NUMERICAL SIMULATIONS OF HYPERVELOCITY IMPACT EXPERIMENTS INVOLVING SINGLE PLATES AND SINGLE WHIPPLE BUMPER SHIELDS

David F. Medina
Scott R. Maethner

October 1993

Final Report

APPROVED FOR PUBLIC RELEASE; DISTRIBUTION IS UNLIMITED.

93-26417

PHILLIPS LABORATORY
Advanced Weapons and Survivability Directorate
AIR FORCE MATERIEL COMMAND
KIRTLAND AIR FORCE BASE, NM 87117-5776

93 11 1 0-5

This final report was prepared by the Phillips Laboratory, Kirtland Air Force Base, New Mexico, under Job Order SNL0AH01. Dr. Firooz A. Allahdadi (WSSD) was the Phillips Laboratory Project Officer-in-Charge.

When Government drawings, specifications, or other data are used for any purpose other than in connection with a definitely Government-related procurement, the United States Government incurs no responsibility or any obligation whatsoever. The fact that the Government may have formulated or in any way supplied the said drawings, specifications, or other data, is not to be regarded by implication, or otherwise in any manner construed, as licensing the holder, or any other person or corporation; or as conveying any rights or permission to manufacture, use, or sell any patented invention that may in any way be related thereto.

This report has been authored by employees of the United States Government. Accordingly, the United States Government retains a nonexclusive royalty-free license to publish or reproduce the material contained herein, or allow others to do so, for the United States Government purposes.

This report has been reviewed by the Public Affairs Office and is releasable to the National Technical Information Service (NTIS). At NTIS, it will be available to the general public, including foreign nationals.
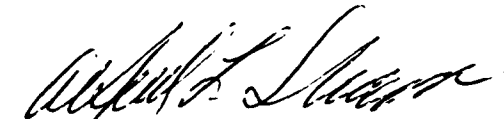
If your address has changed, if you wish to be removed from our mailing list, or if your organization no longer employs the addressee, please notify PL/WSSD, Kirtland AFB, NM 87117-5776 to help maintain a current mailing list.

This technical report has been reviewed and is approved for publication.

FIROOZ A. ALLAHDADI, Ph.D.
Chief, Space Kinetic Impact and Debris
  Branch

FOR THE COMMANDER

ALFRED L. SHARP, GM-15, DAF
Chief, Space Survivability Division

BRENDAN B. GODFREY
Acting Director, Advanced Weapons
  and Survivability Directorate

REPORT DOCUMENTATION PAGE

1. AGENCY USE ONLY (Leave blank)	2. REPORT DATE October 1993	3. REPORT TYPE AND DATES COVERED Final 8 Jun 92 - 3 Sep 92

4. TITLE AND SUBTITLE	5. FUNDING NUMBERS
NUMERICAL SIMULATIONS OF HYPERVELOCITY IMPACT EXPERIMENTS INVOLVING SINGLE PLATES AND SINGLE WHIPPLE BUMPER SHIELDS	PR: SNL0
6. AUTHOR(S) David F. Medina, Scott R. Maethner	TA: AH WU: 01

7. PERFORMING ORGANIZATION NAME(S) AND ADDRESS(ES)	8. PERFORMING ORGANIZATION REPORT NUMBER

9. SPONSORING / MONITORING AGENCY NAME(S) AND ADDRESS(ES)	10. SPONSORING / MONITORING AGENCY REPORT NUMBER
Phillips Laboratory Kirtland AFB, NM 87117-5776	PL-TR--93-1027

11. SUPPLEMENTARY NOTES

12a. DISTRIBUTION / AVAILABILITY STATEMENT	12b. DISTRIBUTION CODE
Approved for public release; distribution is unlimited.	

13. ABSTRACT (Maximum 200 words)

Well-controlled hypervelocity impact experiments, conducted in support of the Space Station Shielding program, were numerically modeled using two sophisticated hydrocodes, the multidimensional hydrodynamics code (CTH) and the Smoothed Particle Hydrodynamics code (SPH). The experiments simulated the impact of space debris on single shields and single Whipple bumper shield plate configurations. Impact velocities on the order of 10 km/s were applied to gram-sized flier plates and spherical projectiles that struck thin (<1 cm) aluminum, titanium, and steel plates. Computational predictions of the debris cloud dynamics and plate damage for these experiments were analyzed and correlated with the data obtained from pulsed laser photographs and high-speed X-ray photography. Computational results of both hydrocodes were compared to each other.

14. SUBJECT TERMS Whipple Bumper Shields, Numerical Simulation of Experiment, Hypervelocity Impact, Smoothed Particle Hydrocode, CTH Hydrocode			15. NUMBER OF PAGES 68
			16. PRICE CODE

17. SECURITY CLASSIFICATION OF REPORT Unclassified	18. SECURITY CLASSIFICATION OF THIS PAGE Unclassified	19. SECURITY CLASSIFICATION OF ABSTRACT Unclassified	20. LIMITATION OF ABSTRACT SAR

PREFACE

Accesion For		
NTIS CRA&I		X
DTIC TAB		
Unannounced		
Justification		
By		
Distribution /		
Availability		
Dist	Avail and/or Special	
A-1		

CONTENTS

FIGURES

FIGURES (Concluded)

TABLES

1.0 SUMMARY

Five well-controlled hypervelocity (HV) impact experiments, conducted by Sandia National Laboratories (SNL) Albuquerque, New Mexico, in support of the Space Station Shielding Program, were numerically modeled using two sophisticated hydrocodes: the multidimensional hydrodynamics (CTH) code and the smoothed particle hydrodynamics (SPH) code. Four of these experiments were Whipple shield setups consisting of a standoff shield and witness plate. The intent of the five experiments was to demonstrate the effectiveness of shielded (Whipple) and unshielded plates for protecting spacecraft against orbital debris. Impact velocities in excess of 10 km/s were applied to gram-sized flier plates and spherical projectiles that impacted thin plates (< 1 cm) made of aluminum alloy, titanium alloy, and steel.

In the first pair of Whipple shield experiments (XH-9 and XH-10), the initial parameters were controlled so that the initial conditions of the two experiments were as identical as possible. Any differences between the outcome of the two tests could then be attributed to differences in the characteristics of the flyer plates prior to impact. The materials used were titanium alloy for the stand-off shields (0.07366 cm thick) and witness plates (0.4 cm thick). The projectiles used in the experiment were aluminum flyer plates. The simulations of XH-9 and XH-10 used spherical projectiles.

In the second pair of Whipple shield experiments (WS-11 and WS-12), the objective was to find an optimum Whipple bumper shield configuration for protection against projectiles traveling in excess of 10 km/s. The references list pervious simulations of these experiments using CTH. They were reproduced here using updated constants for the analytical equation of state. Also, the cell size was held constant throughout the computational mesh to avoid numerical problems associated with neighboring cells of dissimilar size or non-square cells. The two experiments were similar in material type and stand-off shield and witness plate thicknesses. There was a large difference in the initial energy of the tests. One experiment had almost twice the initial kinetic energy of the second due mainly to differences in the initial projectile mass. The simulations used both disk-shaped and spherical projectiles.

The primary objective of numerically simulating these experiments was to apply hydrocode modeling as a tool to understand the physical processes that occurred during these HV impacts. A secondary objective was to use the experimental data to test the predictive capability of the hydrocodes and to compare the results of one code to the other. High-speed photographs of

1

some of the experiments, taken at various times during the events, were compared to the numerical calculations and are presented in this report. Physical quantities compared include hole size, debris cloud dynamics, witness plate impact time, and witness plate damage.

The CTH and SPH codes generally predicted similar results when modeling the five HV impact experiments. Predictions from one code for hole size, debris cloud dynamics, witness plate impact time, and plate deformations were all within 20 percent of the other with the exception of XH-9 and XH-10 which produced differences of about 40 percent for radial velocity between the two codes.

Qualitatively, the codes modeled these impacts very well. In all cases the responses of the projectile, stand-off shield, and witness plate correlated well with the experimental results. Quantitative differences in hole size, debris cloud dynamics and witness plate impact time are listed in tabular form.

2.0 INTRODUCTION

The problem of HV debris impacting orbiting space structures is a primary concern relating to the survivability of these structures. A complete assessment of the survivability of space structures to HV impact requires a thorough knowledge of the physical processes that occur during impact. This can be accomplished by conducting well-controlled laboratory experiments and by numerically simulating the impacts with high fidelity hydrocode calculations that incorporate the appropriate material equations of state and material models. Currently, the experimental state of the art for HV impact analysis is limited to in-flight photographs and postimpact debris characterization. On the other hand, hydrocode simulations of HV impacts provide a reliable means to track the multitude of intervening processes that occur and have been shown to correlate well with experiments for a variety of impact problems[*] (Refs. 1-3). It is well accepted that experimental analysis is enhanced through the use of hydrocode simulations which in turn are improved through comparison to experimental data. Both contribute to the assessment of space structure survivability.

Defending against the orbital debris threat has become an important engineering design challenge. Providing adequate protection while minimizing the spacecraft weight has lead to many innovative shielding concepts. For example, shielding proposals for the Space Station Freedom include the Whipple bumper shield concept. This type of shielding uses a thin plate separated from the hull structure which acts to effectively break up incoming debris. If perforation of the shield occurs, the resulting debris cloud will impact the inner hull over a wider area and a longer time thus producing less damage than an intact projectile would cause. As part of the validation and concept demonstration of shielding for the Space Station Freedom, SNL has conducted five well-controlled laboratory experiments to investigate the debris environment and plate damage resulting from impacts of HV projectiles onto shielded and unshielded thin plates.

These five experiments[**,+] (Ref. 4) have been modeled using two sophisticated hydrocodes: The

---

[*] Maethner, S. R. and Amdahl, D. J., **Hypervelocity Impact Calculations Using Smoothed Particle Hydrodynamics**, Unpublished report, Phillips Laboratory, Kirtland AFB, NM.

[**] Unpublished report for experiments XH-9 and XH-10, Sandia National Laboratories, Albuquerque, NM, 1993.

[+] Results of experiment HOLO17 are to be published by Ang, J., **Pulsed Holograph for Hypervelocity Impact Diagnostics**, *Int. J. Impact Engineering.* Vol 14, 1993.

3

CTH code (Ref. 5) and the SPH code (Refs. 6 and 7). The calculations in this report serve primarily to understand the interaction and physical processes involved in this type of impact and secondarily as a validation of the codes. Specifically, the objectives of this study are to

- improve the understanding of the complex phenomena that occur when HV projectiles impact and penetrate thin target layers and form debris clouds

- apply an experimental data base for current and future code benchmarking and validation

- extend the ability to use both experimental and theoretical tools for the analysis of HV impact, and the design and optimization of stand-off shields

- describe the discrepancies between experimental and numerical simulations to identify shortcomings of the modeling techniques so that the predictive capability and limitations of the codes for this class of problems can be understood and improved.

3.0 BACKGROUND

The experiments modeled can be classified as a subset of thin shield normal HV impacts in which the projectile completely passes through the shield and breaks up (Ref. 8). During these impacts, the projectile penetrates a thin stand-off shield, fragments as it passes through that shield, and continues to travel as an expanding debris cloud which may, in turn, impact a secondary structure, which in this case is the witness plate.

The effectiveness of a stand-off shield to protect secondary structures depends on its ability to break up the projectile into small fragments that are spread radially, many of which are at velocities below that of the original projectile. The leading edge of the debris cloud, which usually consists mostly of shield material, will generally travel at velocities higher than that of the original projectile for certain types of material and may undergo changes in phase to liquid or gas for high velocity impacts. The degree to which the projectile breaks up, melts, or vaporizes depends primarily on the impact velocity, material strength, and shield thickness.

The level of fragmentation in the debris cloud and its expansion properties are important in assessing the damage produced on secondary structures. If a secondary structure happens to be the inner hull of a spacecraft, it becomes critical that it is not penetrated by the debris cloud. Penetration may lead to severe interior component damage and possible mission failure. After the projectile passes through the shield, it and a portion of the shield will generally travel in the original direction of the projectile. A debris cloud that contains a fragmented projectile is less damaging to a secondary structure than one that contains a relatively intact projectile because it will deposit its energy over a wider area and over a longer duration.

4.0 MODELING APPROACH

A summary of the five experiments modeled using both of these hydrocodes is presented in Table 1. The experiments involved normal HV impacts of single and shielded thin plates by spherical and disk-shaped projectiles. Disk-shaped flyer plates were used for the experiments with impact velocities on the order of 10 km/s. Due to the high pressures required to accelerate the flyer plates to high velocities, the flyer plates were slightly deformed and were at varying angles of yaw prior to impact.

Figure 1 depicts the general setup of the five experiments. This figure also defines terminology used for describing the dimensions associated with this general setup and the dynamic processes that occur during impact. When comparisons are made between the CTH and SPH calculations and between the CTH and SPH calculations and the experiments, several terms are used to describe the dynamics of the debris cloud such as length, width, and average velocity. Measured values obtained from experimental photographs were subject to error associated with blurred images and impact flash. Debris cloud length (l) refers to the distance the leading edge of the debris cloud has traveled from the inside surface of the stand-off shield at a given time. Debris cloud width (w) refers to the total distance of expansion of the debris cloud in the radial direction at a given time. Average radial velocity is determined by dividing one half the width of the debris cloud by the time elapsed since impact. Similarly, average axial velocity is determined from the length of the debris cloud at a given time.

Comparisons between experimental and numerical results are restricted to four physical quantities: (1) hole size in the stand-off shield, (2) time of witness plate impact, (3) debris cloud dynamics, and (4) witness plate damage. The diameter of the hole produced in the stand-off shield by the projectile was measured at various times for each numerical calculation. For the experiments described in this report, the hole in the stand-off shield could be estimated in one experimental photograph. In the numerical calculations, the growth rate of the hole levels off shortly after perforation (at about 20 μs). Results of an empirical model, described by Kinslow (Ref. 8), that predicts hole size in thin plates from spherical projectiles was compared to the values obtained from the hydrocode calculations. This empirical model was developed based on data from numerous experiments using thin aluminum shields. The projectiles in these experiments were aluminum spheres that were given initial velocities ranging from 1 to 8 km/s. This model was found to produce good results for dissimilar shield and projectile materials. The formulation is $D/d = 0.45v(t_s/d)^{2/3} + 0.90$, where D is the hole diameter, d is the spherical projectile diameter, v

Table 1. Matrix of events to be modeled using CTH and SPH.

	HOLO17	XH-9	XH-10	WS-11	WS-12
Projectile:					
Velocity, km/s	4.22	9.72	9.47	10.5	10.1
Material	Stainless Steel	Ti6 Al4V	Ti6 Al4V	Aluminum 6061-T6	Aluminum 6061-T6
Disk thick, cm	None	0.098	0.1044	0.0959	0.0868
Disk diam., cm	None	1.2629	1.2658	1.26	1.9
Sphere diam, cm	0.635	0.6113	0.6237	0.608	0.773
Density, g/cm^3	7.9	4.42	4.42	2.7	2.7
Mass, g	1.06	0.52878	0.56157	0.318	0.653
Stand-off Shield:					
Material	Stainless Steel	Ti6 Al4V	Ti6 Al4V	Aluminum 6061-T6	Aluminum 6061-T6
Density, g/cm^3	7.9	4.42	4.42	2.7	2.7
Thickness, cm	0.063	0.07366	0.07366	0.127	0.127
Witness Plate:					
Material	None	Aluminum 6061-T6	Aluminum 6061-T6	Aluminum 2219-T87	Aluminum 2219-T87
Density, g/cm^3	None	2.7	2.7	2.8	2.8
Thickness, cm	None	0.40132	0.40386	0.3175	0.3175
Stand-off gap, cm	None	15.24	15.24	11.4	11.4
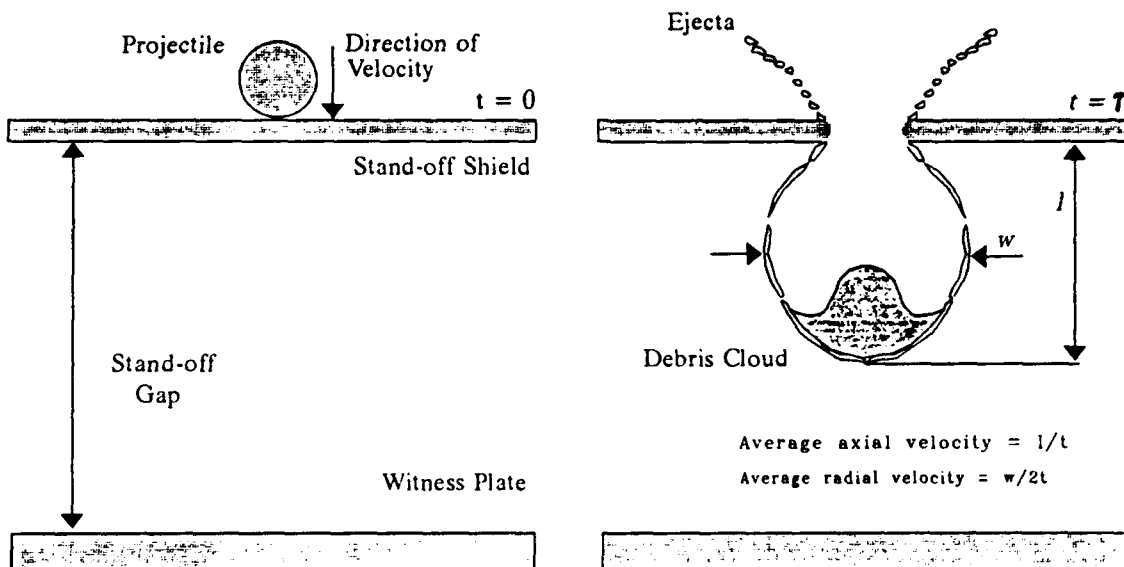
Figure 1. General experimental setup and debris cloud dynamics definitions.

Average axial velocity = l/t

Average radial velocity = $w/2t$

is the velocity of the projectile in kilometers per second, and t_s is the target thickness The target thickness to projectile diameter ratios ranged from 0.040 to 0.504 for the five experiments and were within the range of the empirical formulation.

The second area of comparison, witness plate impact time, is the time at which the debris cloud first hits the witness plate (t = 0 is the time at which the projectile first contacts the stand-off shield). This was determined from the numerical calculations when tracer points (Lagrangian monitoring points) that were placed in the witness plate first showed nonzero values for velocity. Experimental values of the time of impact of the witness plate were estimated from the high-speed photographs and flash X-ray images.

The third area, debris cloud dynamics, refers to the average velocity of the axial and radial components of the debris cloud as defined previously and depicted in Figure 1. These values of velocity were determined from the numerical calculations by directly measuring the length and width of the debris cloud from the material plots. For the experiments, these values were estimated based on the position of the debris cloud with respect to a reference image at known times.

The final area of comparison, witness plate damage, is assessed in a number of ways. For the numerical calculations, the plate damage was obtained from material plots by measuring the displacement of the deformed portion of the plate relative to its initial position. A second approach was to analyze the velocity and displacement of the tracer points in the plate. For some of the experiments, only a qualitative assessment of plate damage could be obtained from the photographs.

5.0 HYDROCODE SETUP REQUIREMENTS

The motivation for modeling these experiments using two separate hydrocodes (CTH and SPH) was to compare the results of two types of numerical algorithms to the experimental results. Also, the results of one code could be compared to the other.

For both CTH and SPH, all projectiles were modeled as spheres of diameters given in Table 1. Although experimental flyer plates exhibit preimpact irregularities which are difficult to model numerically, WS-11 and WS-12 were also simulated using disk-shaped projectiles without attempting to include these irregularities. The spherical projectiles used in the numerical calculations were equivalent in mass to the corresponding flyer plates used in the experiment. All stand-off shields were made at least 8 cm in diameter and all witness plates were given a length of 18 cm in diameter. Plate thicknesses and configurations are summarized Table 1.

To track the calculated dynamic response of the stand-off shields and witness plates, 12 Lagrangian tracer points were placed in the stand-off shield and the witness plate in the manner outlined in Figure 2. The motivation for using Lagrangian tracer points in the stand-off shield was to track the propagation of stress waves along its thickness and length. The resolution of the mesh and particles in CTH and SPH were purposely made fine to allow gradients of stress, velocity, position, internal energy, and temperature to be calculated along the thickness and length. This was done by ensuring that the smallest thickness in each calculation had at least four cells (CTH) or particles (SPH). The tracers along the witness plate were used to track various physical parameters that occurred when the debris cloud impacted the witness plate.

The computational resources required for each hydrocode should be mentioned. The CTH has larger memory requirements than SPH (Eulerian codes generally have greater memory requirements than Lagrangian codes). For the calculations described in this report, all CTH runs that used a fine mesh required the extensive memory resources of the Phillips Laboratory Cray2, while all SPH calculations were easily run on a 64-Mbyte workstation at a considerably less cost. Code-specific details on the initial setup of the CTH and SPH input files are described in Subsections 5.1 and 5.2.

9
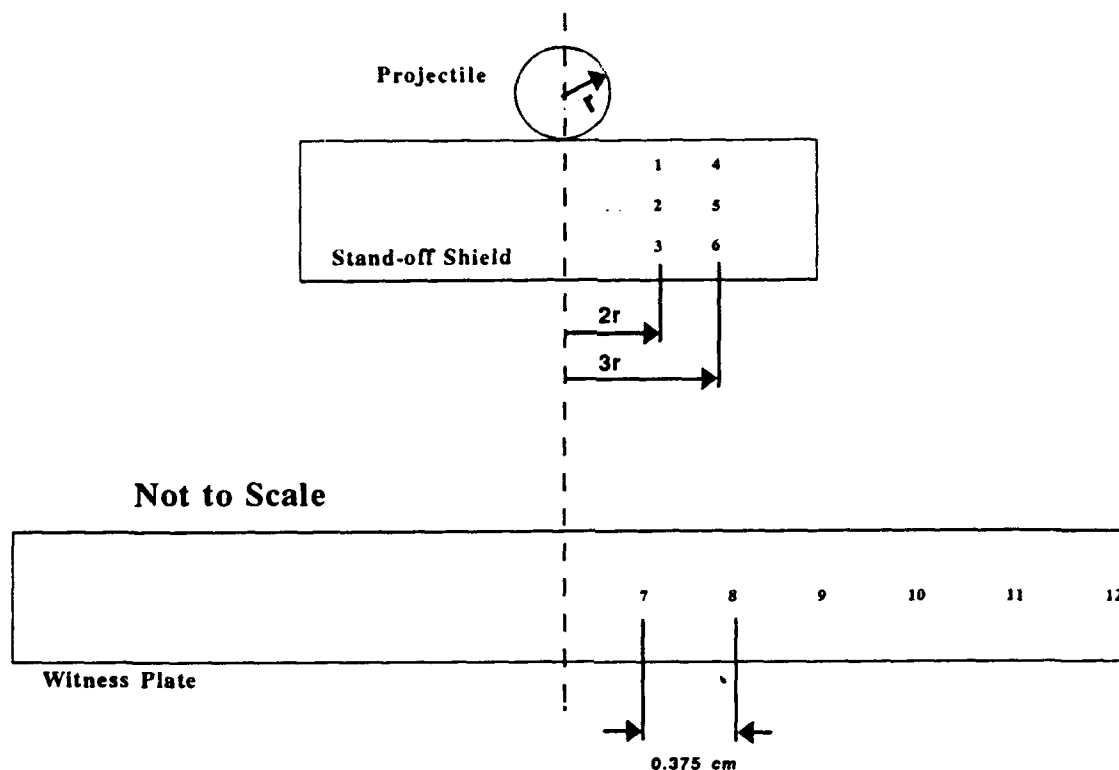
Figure 2. Location of Lagrangian tracer points.

5.1 SETUP OF CTH INPUT FILES

Characteristics that were common to each of the CTH input files for all calculations included cylindrical 2-D coordinates (half-plane symmetry), a minimum of four cells through the thinnest dimension, and the analytical equation of state (ANEOS) using material constants either from the built-in ANEOS library in CTH or those that were modified to match the specific materials used in the experiment. Material constants chosen for each material are shown in Table 2.

Modeling thin plates requires a large number of computational cells to produce an accurate solution. In addition to the fine-meshed calculation, a series of coarse-meshed (one cell through the thinnest dimension) calculations were run. The results of using such a coarse mesh are unacceptable when compared to the results from calculations that use a mesh with at least four cells through the thinnest dimension. Debris cloud shape, propagation velocities, and mass distributions predicted by the calculations using a coarse mesh diverge further from the experimental results than the finer-meshed calculations. The fine-meshed calculation produces a debris cloud that is qualitatively much more similar to photographs of the experiment.

10

Table 2. CTH material constants.

Material	Yield strength (Mbars)	Fracture Strength (Mbars)	Density (g/cc)
2019-T851 Aluminum	0.00352	0.007/0.017[a]	2.8
6061-T6 Aluminum	0.002758	0.0035/0.017[a]	2.7
Steel (STL)	J-C model	0.012	7.9
Ti6Al4V (TI6)	0.012	0.9/0.0508[a]	4.42

[a]These fracture strengths are based on experimental data (Ref. 9) and became available for the calculation of WS-11 and WS-12 using flyer plates.

The fracture model used for each calculation is based on a maximum principal stress threshold. A value for the "fracture strength" is input for each material. If this value is exceeded during the process of the calculation, the deviatoric stresses are set to zero and the material in that cell "fails." No damage history is retained by this fracture model. Further details on the CTH input files are included in Subsections 6.1.2, 6.2.2, 6.3.2 and 6.3.3 which are the descriptions for each of the CTH calculations.

5.2 SETUP OF SPH INPUT FILES

All experiments modeled with SPH used the Mie-Grüneisen equation of state, a minimum pressure fracture model (zero minimum pressure), and an elastic perfectly plastic constitutive model. Table 3 gives the constants for all the materials modeled. All calculations were run in half-plane symmetry using cylindrical coordinates. All calculations used an initial particle size (smoothing length) that depended on the thinnest dimension of the problem. Further details on the SPH input files, including total number of particles used, can be found in Subsections 6.1.3, 6.2.3, and 6.3.4. The calculations were set up so that nine particles spanned the stand-off shield thickness. However, for the witness plate calculations, the witness plate was given a particle resolution half the value of that given to the projectile and the stand-off shield. This allowed the calculation to be run with a smaller number of particles (hence, a smaller calculation time) while maintaining a sufficient number of particles across the thickness of the witness plate.

Table 3. SPH material constants.

Material	Yield Strength (Mbars)	Shear Modulus (Mbars)	Reference State Sound Speed (km/s)	Density (g/cc)	Hugoniot Slope
Aluminum (AL)	0.00055	0.25	5.35	2.71	1.497
Steel (STL)	0.006	0.77	4.58	7.89	1.49
Ti6Al4V (TI6)	0.012	1.0687	4.99	4.42	1.25

11

5.3 CALCULATION OF DEBRIS CLOUD AND EJECTA DIVERGENCE

A single HV impact of a thin shield will produce two forms of debris motion. The first takes the form of a debris cloud that expands along the original path of the projectile, while the second takes the form of an ejecta cone that propagates away from the plate in a direction opposite that of the original motion of the projectile. The degree to which secondary structures are affected by emerging debris from an initial impact of a thin shield depends on the spread (or divergence) of the debris cloud and possibly the ejecta (depending on the orientation/shape of the secondary structure). To quantify these two forms of debris motion, two types of divergence angles are used. The angle δ describes the divergence of the debris cloud and the angle ϵ describes the divergence of the back ejecta cone. These angles are defined in Figure 3. The impact of the diverging debris cloud on a parallel secondary structure (e.g., a witness plate) will be spread over an area given by $\pi d^2 \tan^2(\delta/2)$, where d is the distance from the stand-off shield to the secondary structure.
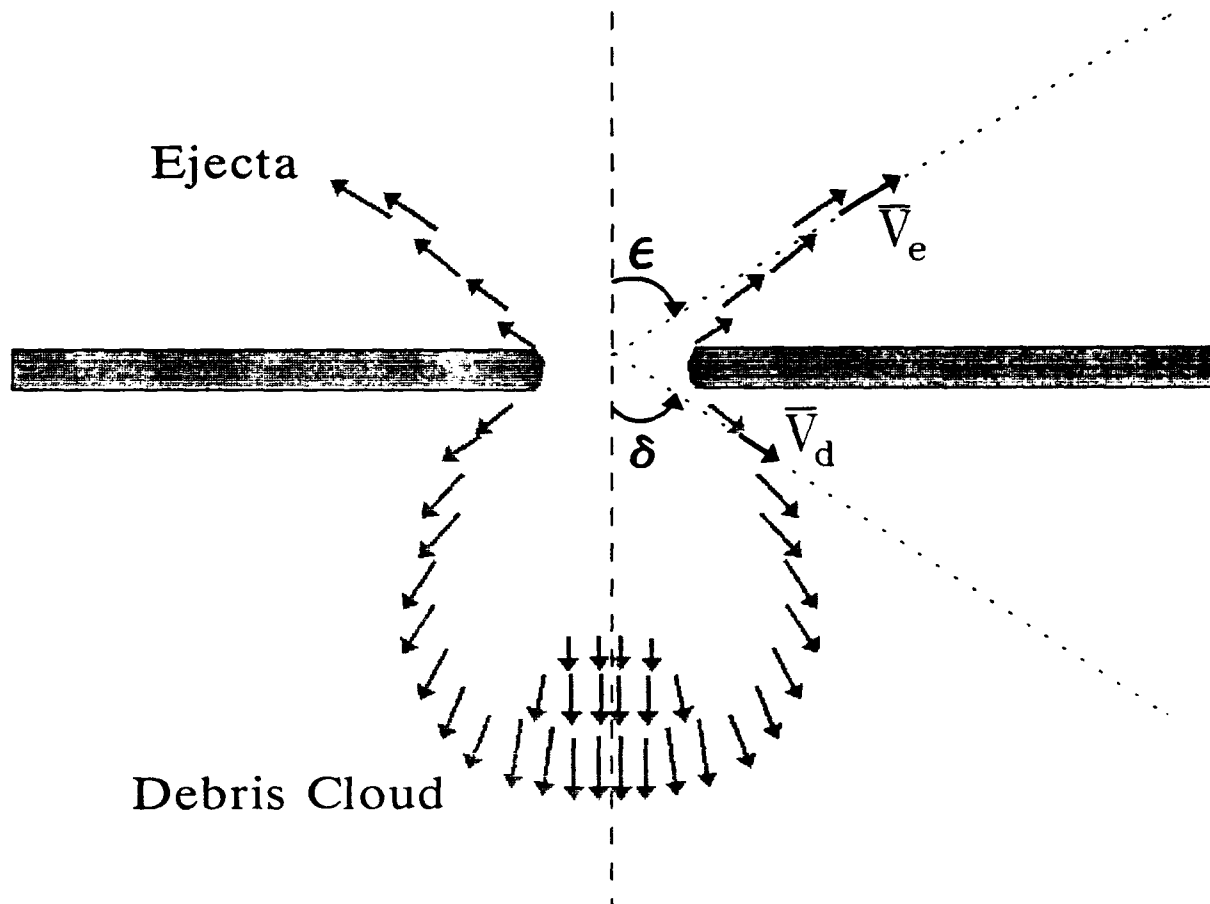
Figure 3. Calculation of debris cloud and ejecta divergence.

6.0 COMPUTATIONAL RESULTS

6.1 EXPERIMENT HOLO17

6.1.1 Description of Experiment HOLO17

In the HOLO17 experiment, a steel sphere impacted a thin steel target of thickness one-tenth that of the projectile diameter (0.635 cm) at a velocity of 4.22 km/s (Table 1). The intent of this experiment was to produce a debris cloud that was undisturbed by a secondary structure. This allowed one to analyze the cloud for shape, propagation, divergence, and fragment spatial distribution. A pulsed laser photograph was taken at 22 µs after impact (Fig. 4). The numerical simulations for this experiment are described in Subsections 6.1.2 and 6.1.3.
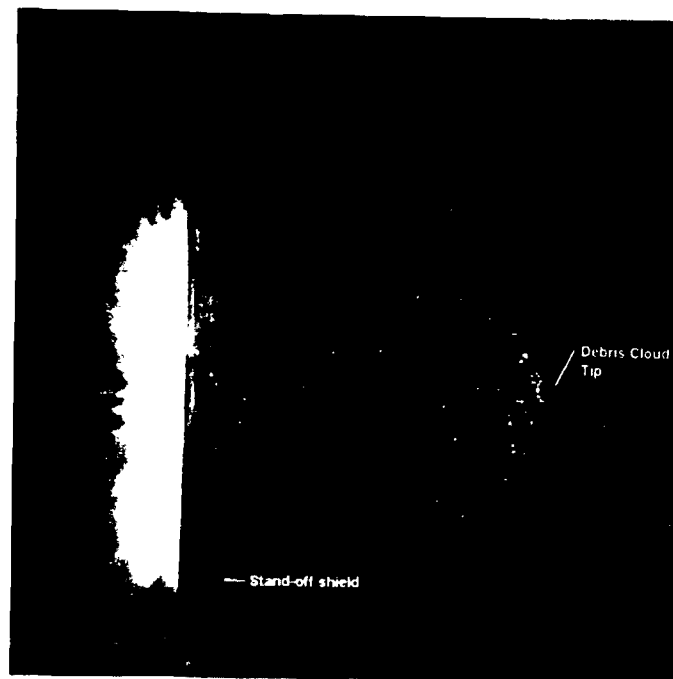
Figure 4. Pulsed laser photograph of HOLO17 at 22 µs.

13

6.1.2 CTH Results for HOLO17

A resolution of six cells along the thinnest dimension was used for this calculation. The result at 22 μs for the CTH HOLO17 calculation is shown in Figure 5. This figure shows the entire debris cloud and a closeup view of the debris cloud tip. The shape of the debris cloud in the experiment can be compared directly to this figure. The width-to-length ratio of the cloud at 22 μs calculated by CTH was 0.8 while the cloud in the experiment had a ratio of 0.812. Although the overall shape was similar, there were differences in the length and width dimensions (hence, differences in axial and radial velocities). The CTH code calculated an axial velocity of 3.35 km/s while the experiment showed an axial velocity of 5.26 km/s. Radial velocity was 1.68 km/s for the experiment versus 2.14 km/s for the calculation. Debris cloud characteristic dimensions for both the HOLO17 experiment and corresponding calculation are listed in Table 4.

Total mass in the debris cloud at 22 μs was calculated by summing the mass in each computational cell located slightly downstream of the inside surface of stand-off plate. The total mass in the debris cloud was found to be 1.058 g (90.2% projectile mass and 9.8% shield mass). Since the initial mass of the projectile was 1.06 g, one should expect more mass than this in the debris cloud. This discrepancy is likely to be due to numerical imprecision since a coarser-meshed calculation (four cells through the thinnest dimension) calculated 0.38 g of mass in the debris cloud which is even less consistent with initial conditions. Also, it was found that mass in the debris cloud may vary by ±0.2 g over a span of 1 μs in the same finely meshed calculation (six cells through the thinnest dimension).

A material plot of the debris cloud at 6 μs is depicted in Figure 6. The average axial velocity was 3.44 km/s and the average radial velocity was 1.77 km/s. At this time the width-to-length ratio of the cloud is 1.03 cm. The ellipsoidal shape of the cloud at 22 μs is a result of the faster axial velocity.

Maximum shear stress history is shown in Figure 7. Peak values for shear stress are 575 MPa at $2r$ and 500 MPa at $3r$. This figure indicates that there is not much change in shear stress along the thickness of the plate at $2r$ or $3r$.

The cloud divergence, δ, and ejecta divergence, ε, as defined in Subsection 4.3 were determined at each microsecond up to 22 μs. By 5 to 10 μs, the angles δ and ε have converged to values of about 80 and 95 deg, respectively.
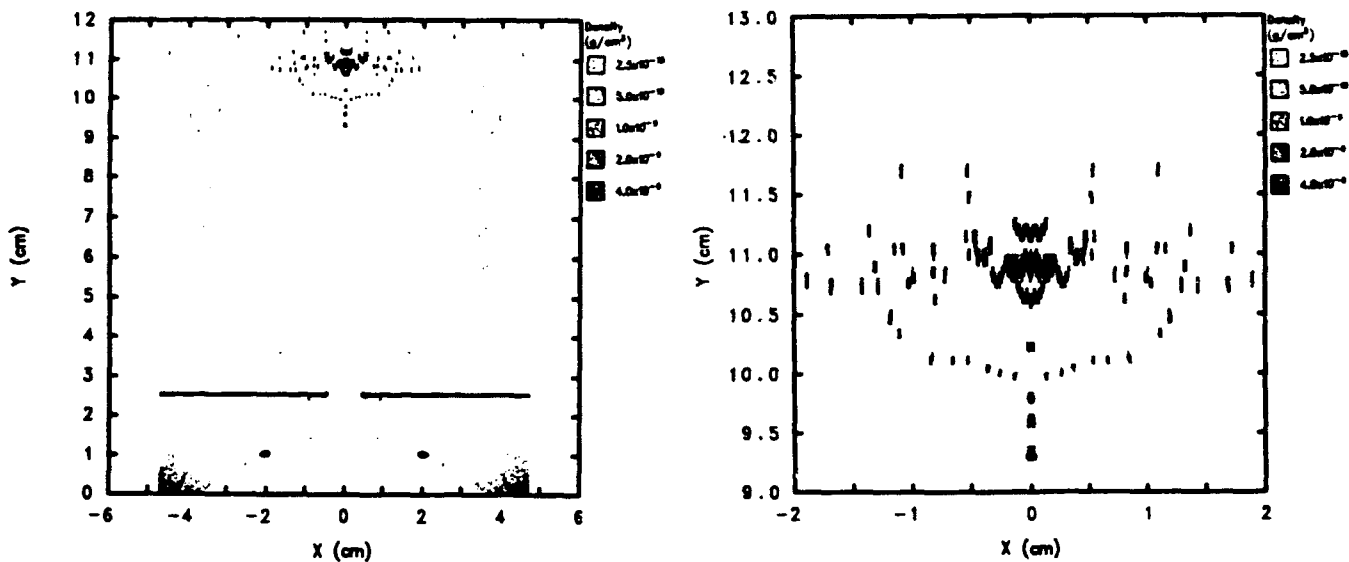
Figure 5. CTH material plots of HOLO17 at 22 μs

Table 4. Dynamic characteristics of experiment and calculations, HOLO17

	HOLO 17		
	CTH	SPH	Experiment
Stand-off Shield Hole Size (cm)			
at 2 μs	0.84	0.90	a
at 6 μs	0.86	0.95	a
at 10 μs	0.86	0.95	a
at 22 μs	0.86	0.95	1.61
Debris Cloud Dynamics			
Length, l (cm)			
at 6 μs	2.25	2.60	a
at 12 μs	4.79	6.35	a
at 16 μs	6.44	7.25	a
at 22 μs	9.20	10.0	11.57
Width, w (cm)			
at 6 μs	2.19	2.20	a
at 12 μs	3.90	4.00	a
at 16 μs	5.25	5.00	a
at 22 μs	7.38	6.80	9.4
Late-Time Divergence Angles (deg)			
Cloud	80	80	68
Ejecta	95	100	92

a Experimental pulsed laser photographs did not provide these data.

15

Figure 6. CTH material plot of HOLO17 at 6 μs.

Figure 7. CTH maximum shear stress plots of HOLO17 at 2r (left) and 3r (right).

6.1.3 SPH Results for HOLO17

The SPH calculation of this experiment was carried out to 22 μs. The experimental pulsed laser photograph shows a debris cloud 11.57 cm long and 9.4 cm wide at 22 μs giving an average axial

16

velocity of 5.26 km/s and an average radial velocity of 2.14 km/s. The SPH calculation shows a slightly smaller debris cloud at this ti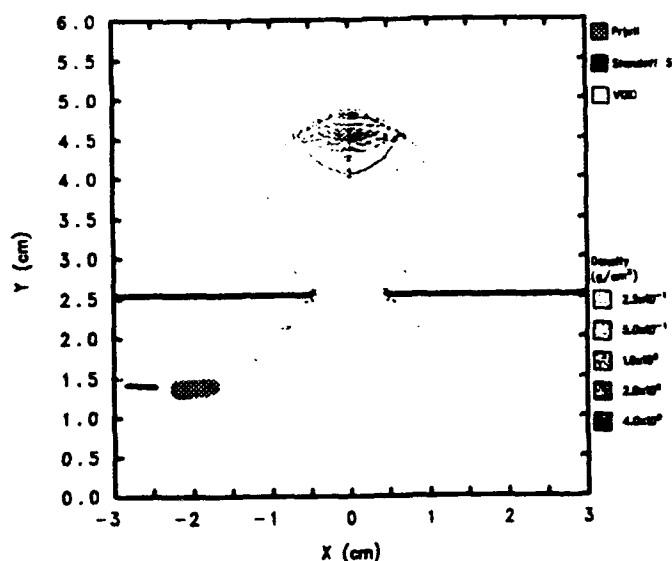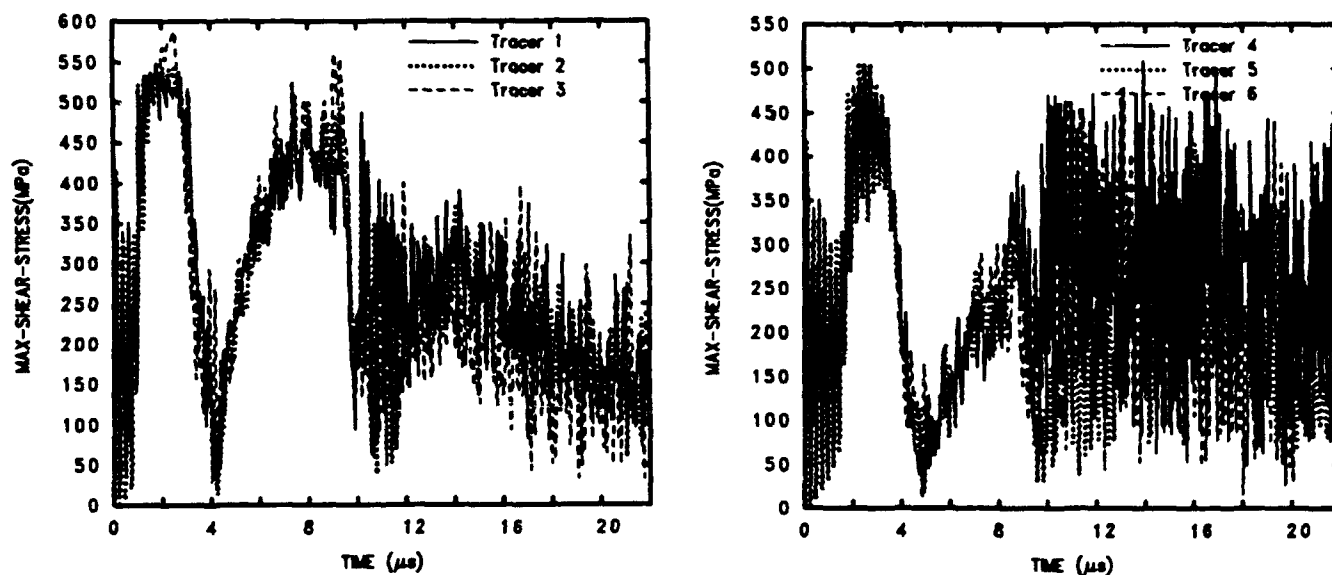me. It predicts a debris cloud that is 10 cm long and 6.8 cm wide, giving an average axial velocity of 4.55 km/s and an average radial velocity of 1.55 km/s. The overall shape of the debris cloud (width-to-length ratio) found in the experiment was 0.812 while the ratio calculated by SPH was 0.68. Figure 8 shows the SPH calculation at 22 μs. The shape of the leading edge of the debris cloud produced in the experiment is slightly flatter than the cloud calculated by SPH. The SPH simulation shows remnants of the projectile in the cloud that extend back from the leading edge. The shape of remnants of this form is not evident in the cloud produced during the experiment, where the projectile remnants coat the inside surface of the cloud's leading edge.

The shape of the debris cloud at an earlier time is more spherical. This can be seen in Figure 9 which shows the calculation at 6 μs. At this time the cloud has an average axial velocity of 4.33 km/s and an average radial velocity of 1.88 km/s. The width-to-length ratio at this time is 0.846.
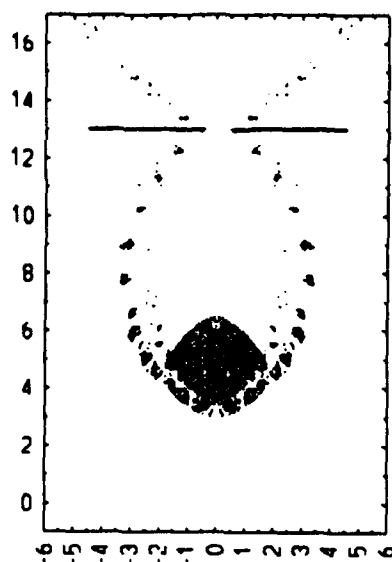
Figure 8. SPH material plot of HOLO17 at 22 μs.
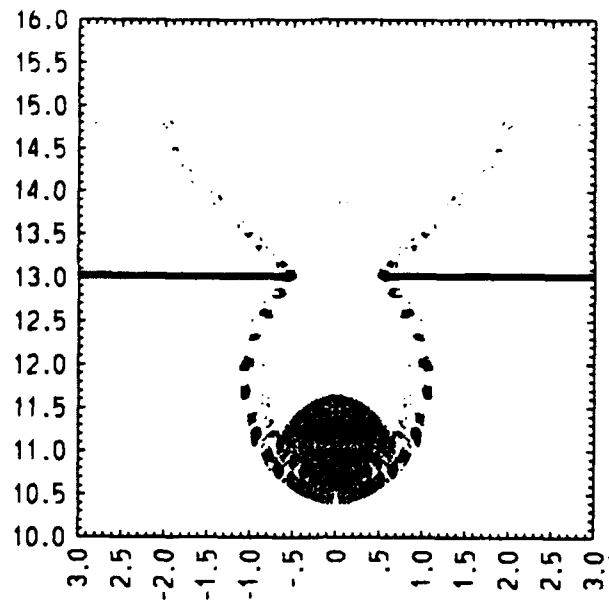
Figure 9. SPH material plot of HOLO17 at 6 μs.

The debris cloud and ejecta divergence angles were determined for the SPH HOLO17 calculation. Figure 10 is a plot of these divergence angles over the calculation time. The cloud divergence converged to a value of 80 deg and ejecta divergence converged to a value of about 100 deg. This indicates that the debris cloud would impact an area of $\pi(0.839)d^2$ cm^2 on a parallel witness plate at a distance, d, from the stand-off shield.
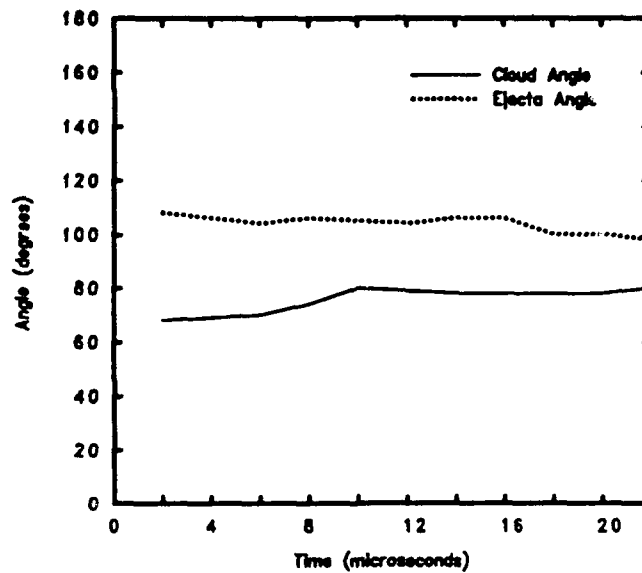
Figure 10. SPH debris cloud and ejecta divergence angles for HOLO17.

6.1.4 Comparison of CTH and SPH Results

To allow for a more precise comparison between CTH and SPH, a plotting routine was developed so that CTH output could be plotted on the same scale used by SPH plotting utility. Figure 11 shows the CTH material plot at 22 μs for HOLO17. Figure 8 is the corresponding SPH plot. Differences in the output of these two codes are found in the axial and radial velocities of the debris clouds. The CTH calculation shows a cloud that has slower axial and faster radial velocities than the cloud produced in the SPH calculations. The CTH calculation predicts axial and radial velocities of 3.35 and 1.68 km/s, respectively. The SPH calculation predicts that the cloud has an axial velocity of 4.55 km/s and a radial velocity of 1.55 km/s. Experimental results showed an axial velocity of 5.26 km/s and a radial velocity of 2.14 km/s. The SPH simulation more closely resembles the experimental results for debris cloud axial velocity (off by 13.5%) while CTH is closer to the experimental results for the radial velocity of the debris cloud (off by 21.5%).

The debris cloud divergence angles for CTH and SPH both converged to an angle of 80 deg. Ejecta divergence for CTH and SPH converged to angles of 95 and 100 deg, respectively. Experimental divergence angles were estimated to be 68 deg for the cloud divergence and 92 deg for the ejecta divergence at 22 μs. The CTH and SPH cloud divergence angles were off from the experimental angle by 18 percent. The CTH calculation more closely matched the ejecta angle estimated from the experiment (off by 3%).

At 22 μs the hole formed in the stand-off shield was 0.95 cm in diameter for SPH calculation and 0.86 cm for the CTH calculation. The pulsed laser photograph only allows for a rough estimate of the experimental hole size at 22 μs which was 1.61 cm. The SPH hole size was 6 percent closer to the experimental result than CTH. The empirical model gives a hole size of 0.83 cm.
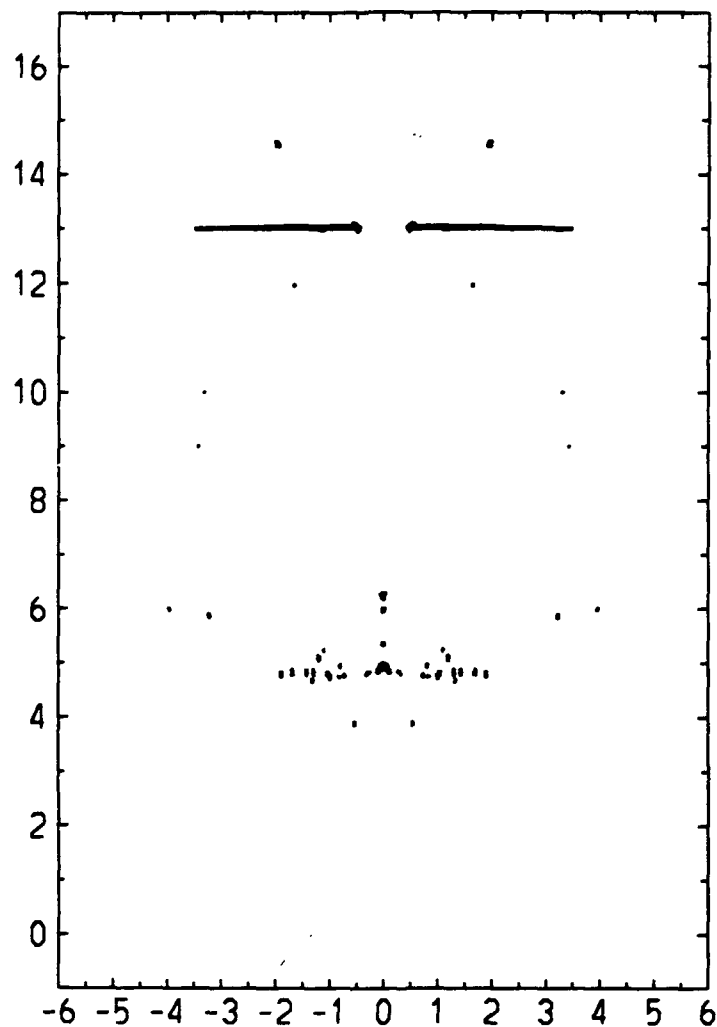
Figure 11. CTH material plot of HOLO17 at 22 μs.

6.2 EXPERIMENTS XH-9 AND XH-10

6.2.1 Description of Experiments XH-9 and XH-10

In the XH-9 and XH-10 experiments, the initial parameters were controlled so that the initial conditions of the two experiments were as identical as possible. Any differences between the outcome of the two tests could then be attributed to differences in the characteristics of the flyer plates prior to impact. The study of this variability from one experiment to the next was the

objective of these experiments. Because of the nature of the projectile launcher, it is difficult to reproduce the same projectile mass, velocity, and yaw angle from one experiment to the next. Preimpact flash X-ray radiographs for XH-9 and XH-10 revealed that there were such differences in the initial mass, velocity, and yaw of the projectile (see Table 1 for values of projectile mass and velocity). This difference in mass and velocity translated into a slight difference in initial energy (kinetic energy). The XH-9 experiment had an initial kinetic energy of 24.7 kJ while the XH-10 experiment had an initial kinetic energy of 26.4 kJ. As shown in Table 1, both tests involved the impact of a titanium alloy projectile into a thin titanium alloy target at velocities of about 10 km/s. An aluminum alloy witness plate was positioned 15.24 cm downstream of the stand-off shield. High-speed framing camera images were taken of both experiments at 5-μs intervals up to 40.5 μs for XH-9 and 34.8 μs for XH-10 (Figs. 12 and 13). The images for these two experiments show different results. The debris cloud in the XH-9 experiment is composed of three distinct regions and is expanding at a rate similar to the debris cloud in XH-10. The three regions are evident in the image of XH-9 at 0.5 μs.

6.2.2 CTH Results for XH-9 and XH-10

Because the stand-off shield in this problem was very thin (0.07366 cm) compared to the inter-plate gap of 15.24 cm, a large number of computational cells were required to maintain the minimum of four cells along the thickness of the stand-off shield. Variable cell size (1.5 percent change) was used in the direction along the axis of symmetry (toward the witness plate). Lower mesh resolution produced significant changes in the qualitative characteristics of the debris cloud.

The calculation of XH-9 was carried out to 21 μs. This was sufficient to see some failure (bending and pitting) in the witness plate (Fig. 14). Due to budgetary constraints, the calculation of XH-10 was only carried out to 10 μs. This did not allow the debris cloud to reach the witness plate. Some comparisons can be made between the two clouds at 10 μs. The XH-10 calculation has a 2.6 percent higher axial and 4.2 percent higher radial velocities than the debris cloud in the XH-9 calculation. Material plots of these debris clouds are shown in Figure 15.

21
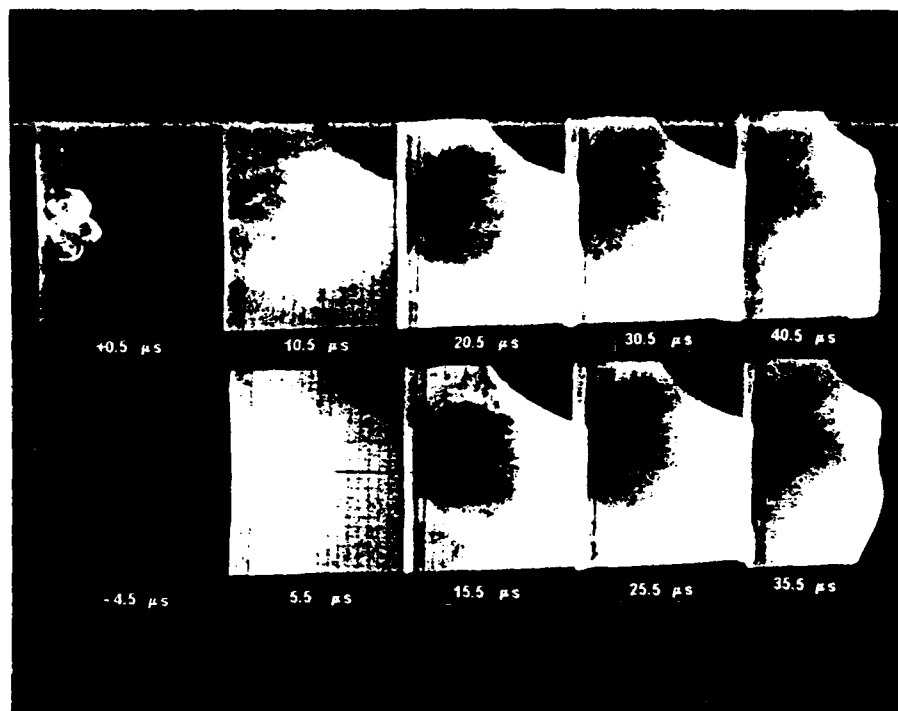
Figure 12. Experiment XH-9, side view.
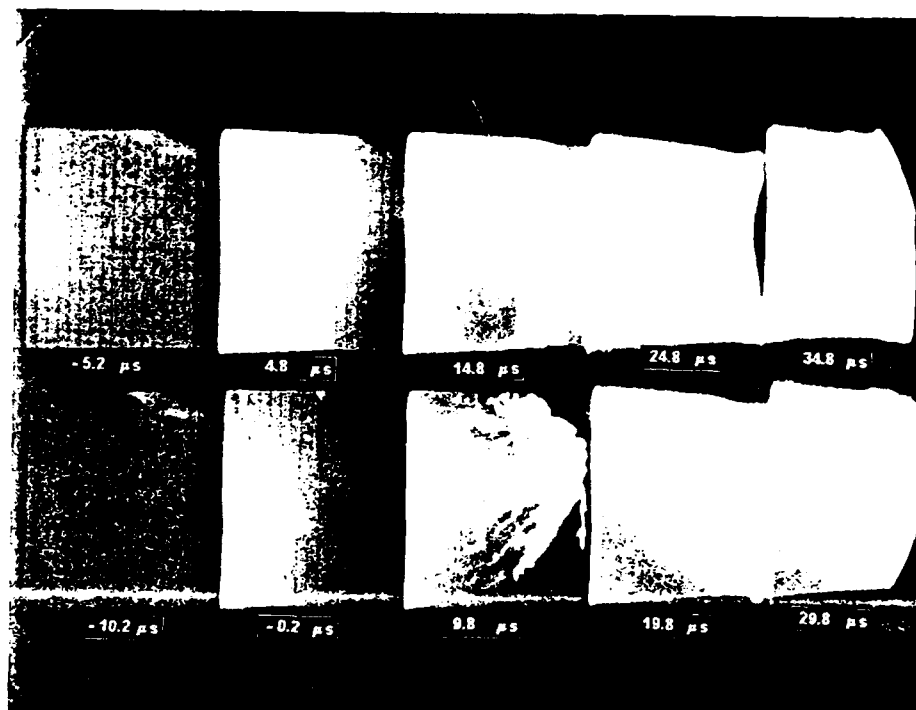
Figure 13. Experiment XH-10, side view.
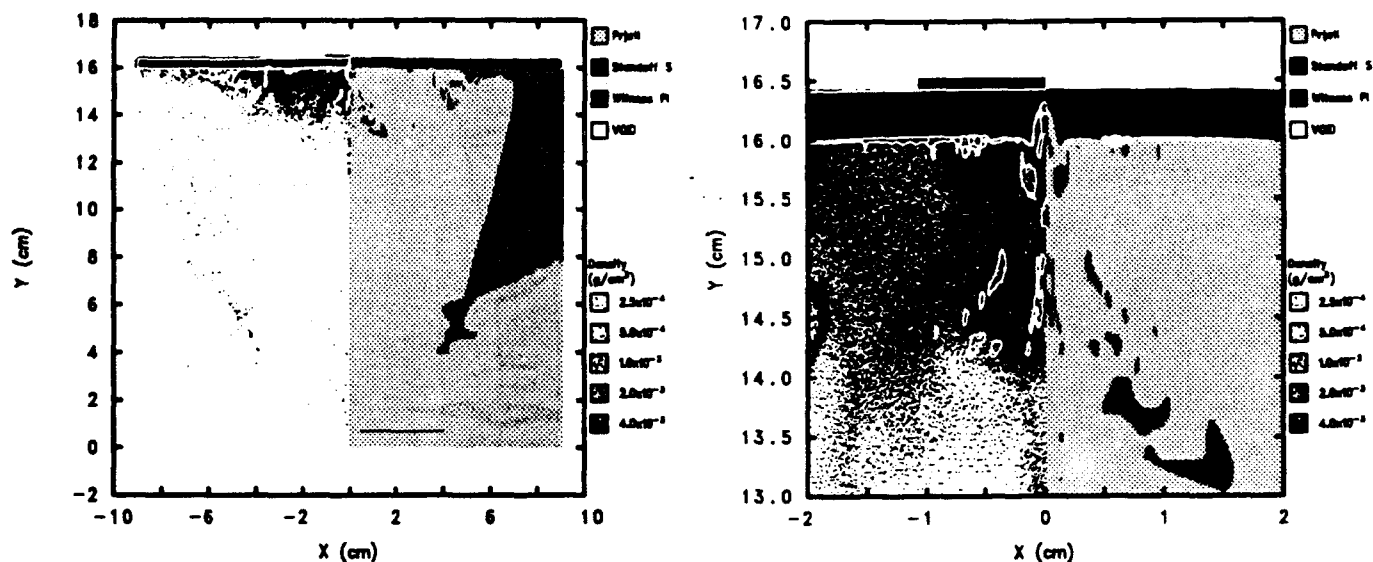
Figure 14. CTH material plots of XH-9 at 21 μs.
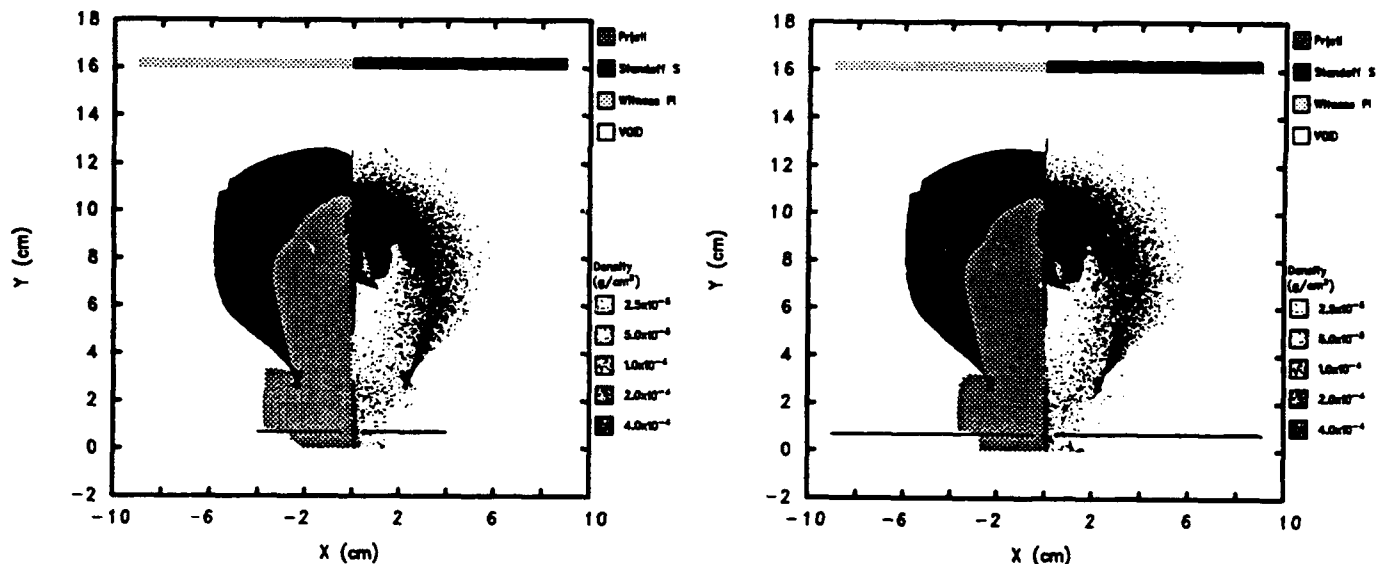
Figure 15. CTH material plots of XH-9 (left) and XH-10 (right) at 10 μs.

A qualitative witness plate damage estimate can be made for the XH-10 debris cloud based on its kinetic energy compared to the XH-9 cloud at 10 μs. Total debris cloud kinetic energy for the XH-10 debris cloud exceeded that of the XH-9 debris cloud by 2.7 kJ (13%) at this time. Thus, it can be assumed that the XH-10 debris cloud would produce more damage to the witness plate. Divergence angles of the debris clouds in XH-9 and XH-10 converged to a constant value of 100 deg. This indicates that these debris clouds would impact areas of 0.1036 m^2 on the respective witness plates.

23

Maximum shear stress was plotted for the witness plate in the calculation for XH-9 (Fig 16).
Maximum shear stress in the witness plate reached a peak value of 200 MPa. Velocity and displacement in the y-direction as monitored by tracers 7, 9, and 11 for XH-9 are shown in Figure 17. These plots are good quantitative measure of the time of witness plate impact (12.5 μs) and the amount of momentum that is transferred to the witness plate. At 21 μs the witness plate has received a peak velocity of 170 m/s and has displaced 0.07 cm.
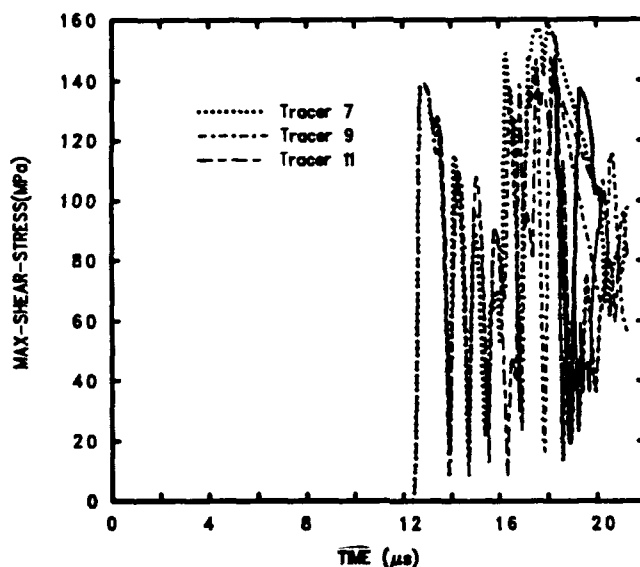
Figure 16. CTH maximum shear stress plot of XH-9 on the witness plate.
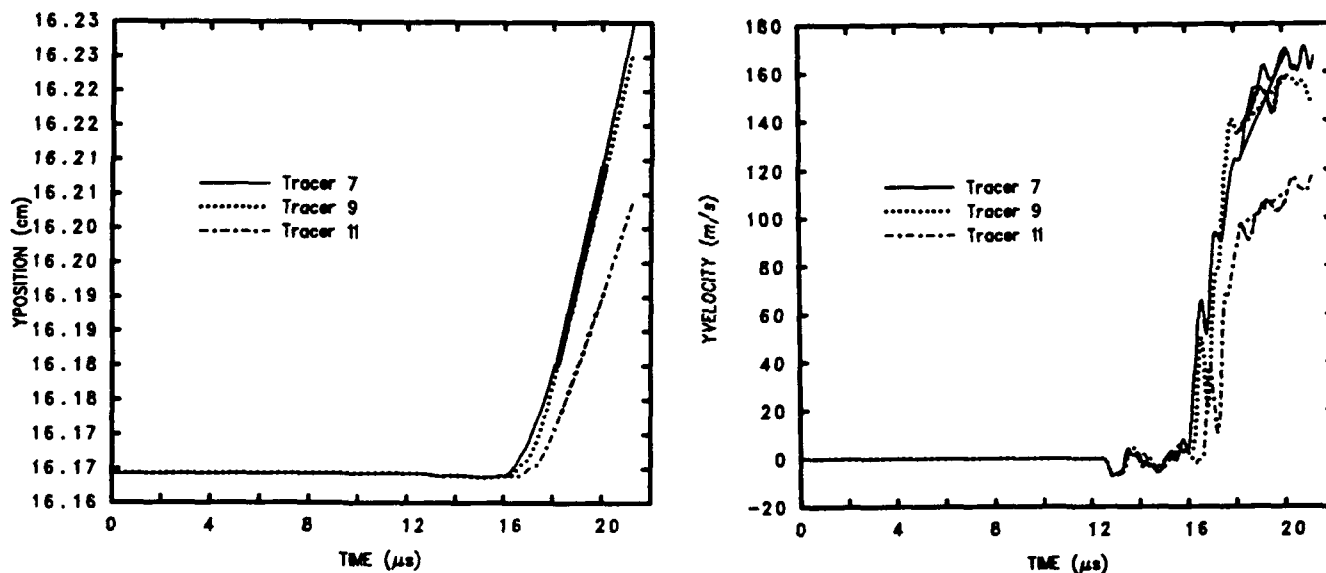
Figure 17. CTH y-displacement and y-velocity plots of XH-9 on the witness plate.

24

6.2.3 SPH Results for XH-9 and XH-10

The SPH simulations of the XH-9 and XH-10 calculations are qualitatively similar. However, slight differences are evident in the damage to the witness plate. This damage is slightly more severe for the XH-10 calculation which is a result of the higher initial kinetic energy of XH-10. The SPH code calculated a larger stand-off shield hole size for XH-10. The debris cloud calculated by SPH for XH-10 had slightly greater axial and radial velocities, impacted the witness plate sooner, and produced slightly greater witness plate damage than the XH-9 calculation. These values are listed in Table 5. The debris clouds for these two calculations at 14 µs are shown in Figure 18.

Debris cloud divergence angles for XH-9 and XH-10 were both 100 deg This indicates that these debris clouds would impact areas of 0.1036 m² on their respective witness plates.

Figure 18. SPH material plots of XH-9 (left) and XH-10 (right) at 14 µs.

Table 5. Dynamic characteristics of experiments and calculations, XH-9 and XH-10.

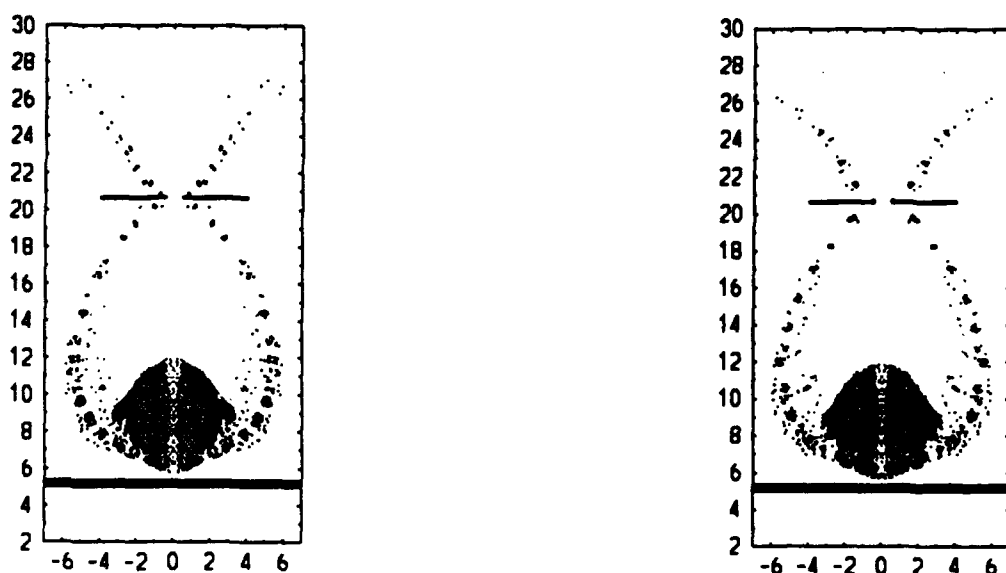|	XH-9			XH-10		
	CTH	SPH	Experiment	CTH	SPH	Experiment
Stand-off Shield Hole Size (cm)						
at 5 μs	0.78	0.90	a	0.97	0.92	a
at 10 μs	0.78	0.90	a	0.99	0.92	a
at 15 μs	0.78	0.90	a	b	0.92	a
at 20 μs	0.78	0.90	a	b	0.94	a
Impact Time (μs)	12.5	14.5	15.8	b	14.4	9.8
Debris cloud dynamics						
Length, l (cm)				Length, l (cm)		
at 5 μs	5.43	5.0	4.8	5.54	5.25	7.78
at 10 μs	11.91	10.5	9.6	12.22	10.65	15.56
Width, w (cm)				Width, w (cm)		
at 5 μs	5.3	4.5	4.75	5.37	4.6	8.16
at 10 μs	11.8	8.5	9.5	12.32	8.7	16.32
Late Time Divergence Angles (deg)				Late Time Divergence Angles (deg)		
Cloud	100	80	a	100	84	a
Ejecta	c	96	a	c	98	a
Witness Plate Damage						
Peak y-Velocity (m/s)				Peak y-Velocity (m/s)		
at 21 μs	170^d	354^e	a	b	359^d	a
Peak y-Displacement (cm)				Peak y-Displacement (cm)		
at 21 μs	0.07^d	0.134^e	a	b	0.1364^d	a

[a] Experimental photographs did not provide this data.

[b] Calculation was terminated prior to this time.

[c] Mesh boundary did not extend to include ejecta.

[d] Tracer 7 on the witness plate.

[e] Tracer 9 on the witness plate.

Two views of the debris cloud witness plate interaction at 21 μs for each calculation are shown in Figures 19 and 20. Figure 19 shows overall and closeup views of the impact for XH-9 at 21 μs. Figure 20 shows similar views for the XH-10 calculation. At 21 μs, there is more damage to the witness plate (increased level of interaction with the debris cloud) for the XH-10 calculation. High-speed framing camera images of the debris cloud were recorded at 5-μs intervals up to nearly 50 μs for both the XH-9 and XH-10 experiments. Experimental debris cloud velocities were estimated from these photographs and are compared to results next.
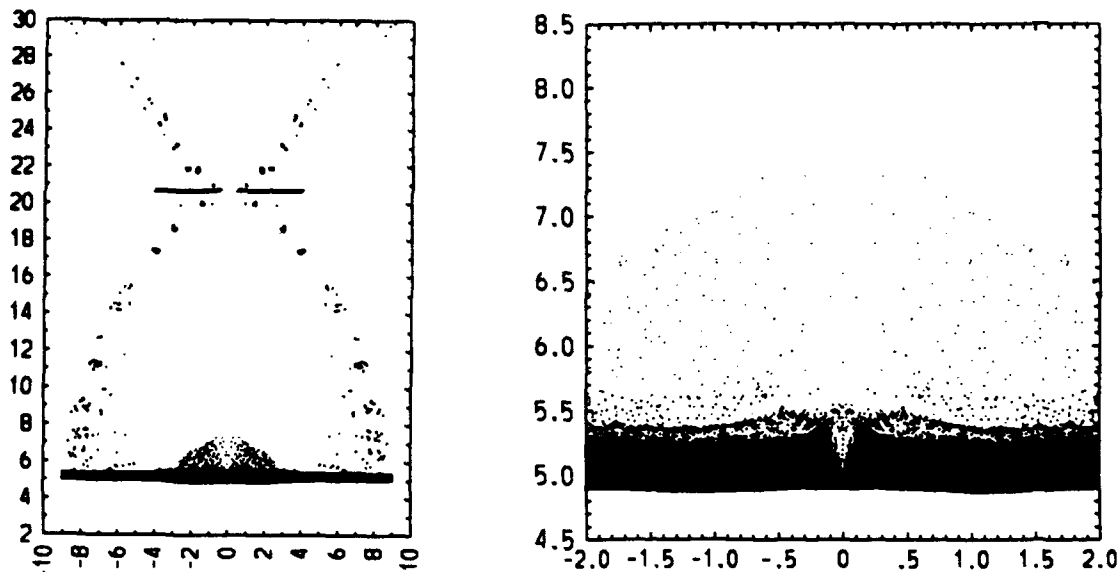
Figure 19. SPH material plots of XH-9 at 21 μs.

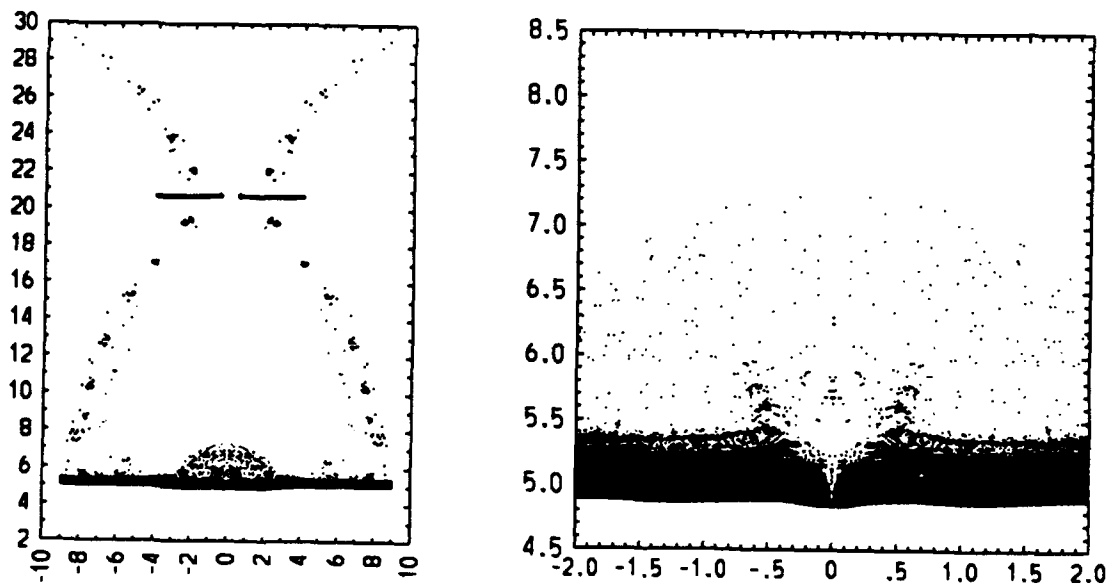Figure 20. SPH material plots of XH-10 at 21 μs.

The debris cloud for the XH-9 experiment was estimated to have an axial velocity of 14.65 km/s and a radial velocity of 8.34 km/s. The debris cloud calculated by SPH had an axial velocity of 10.5 km/s and a radial velocity of 4.25 km/s. Cloud and ejecta divergence angles converged to values of 80 deg and 96 deg, respectively, for the XH-9 calculation.

The debris cloud for the XH-10 experiment appears to have an axial velocity of 15.56 km/s and a radial velocity of 8.16 km/s. The debris cloud calculated by SPH had an axial velocity of 10.7 km/s and a radial velocity of 4.35 km/s. Cloud and ejecta divergence angles converged to values of 84 and 98 deg, respectively, for the XH-10 calculation.

Displacement and velocity in the y-direction and xy stress were plotted as a function of time for tracers 7, 9, and 11 in the witness plate. These plots are presented in Figures 21 through 23. Each figure demonstrates that the witness plates were impacted by the debris cloud at about 14.5 μs for the XH-9 and XH-10 calculations. Tracer 9 for both calculations saw the most action, receiving the largest values of y-displacement, y-velocity, and xy stress. The difference in spacing between tracers 7 and 11 is only 1.125 cm (only about four projectile radii).
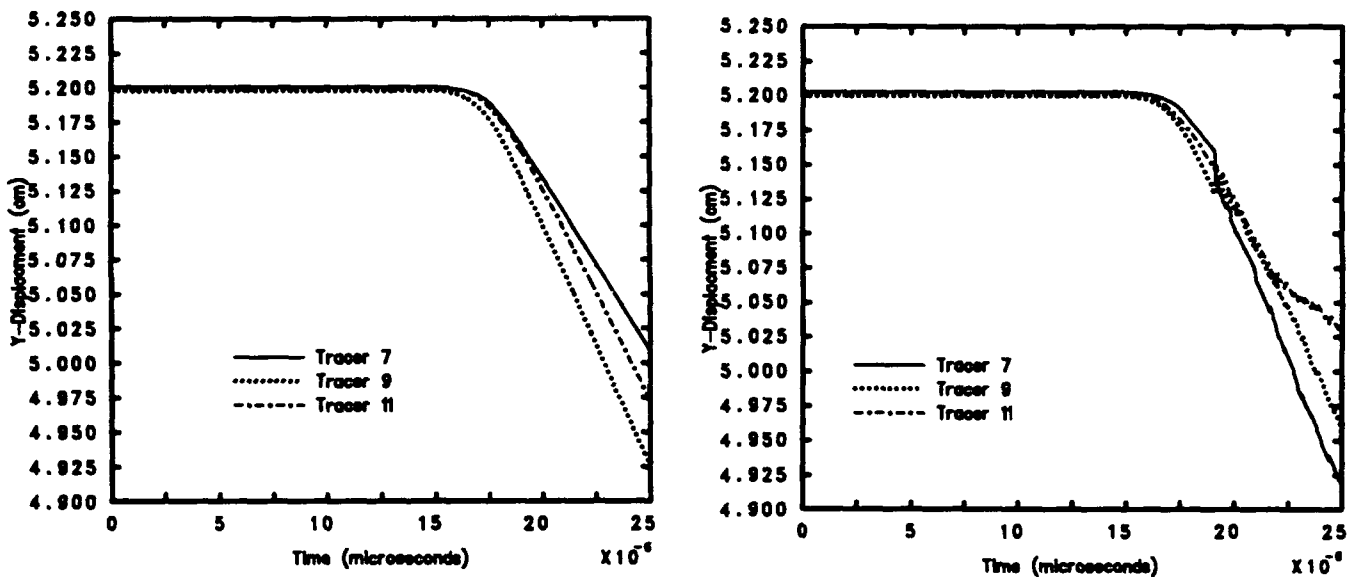
Figure 21. SPH y-displacement plots of XH-9 and XH-10.

28
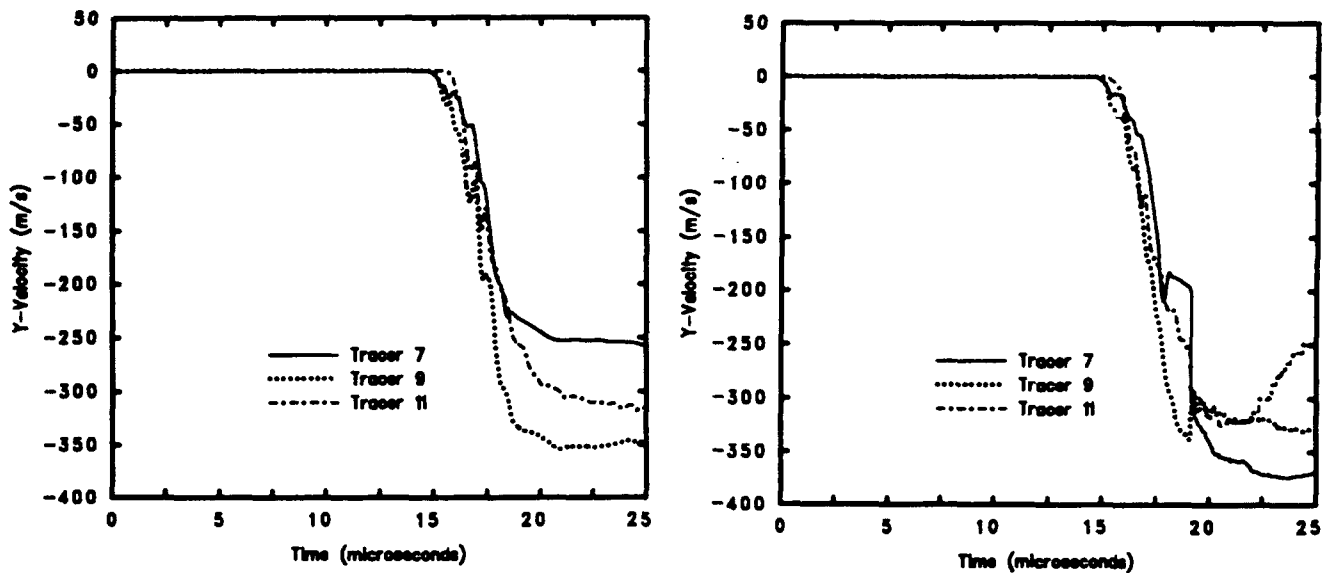
Figure 22. SPH *y*-velocity plots of XH-9 and XH-10.
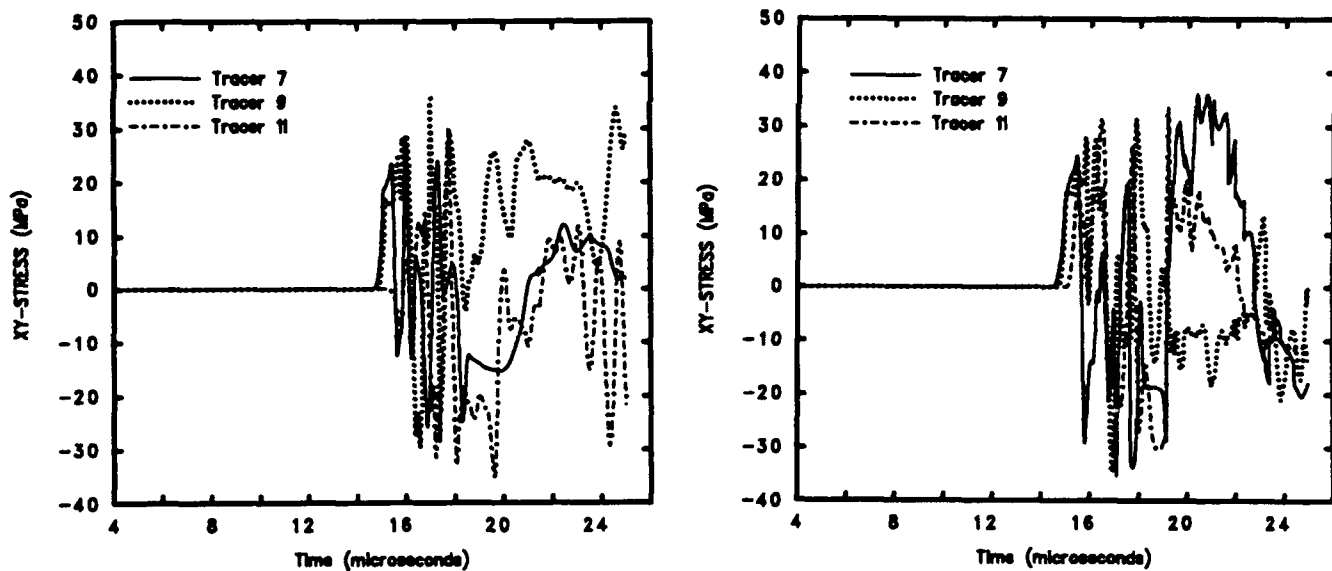
Figure 23. SPH xy stress plots of XH-9 and XH-10.

6.2.4 Comparison of CTH and SPH Results

Several areas were selected for comparing the numerical calculations to the experimental results. These include stand-off shield hole size, witness plate impact time, debris cloud dynamics, and witness plate damage. For all of these, a qualitative measure of the differences is available from

29

the material plots presented earlier. A quantitative measure is obtained from careful measurements of the material plots and from the tracer point data. A discussion of these areas of comparison for experiments XH-9 and XH-10 follows. This information is also presented in Table 5.

The size of the hole formed in the stand-off shield was determined for CTH and SPH calculations of experiment XH-9. At 20 µs, the CTH calculation produced a hole that was 0.78 cm in diameter while the SPH calculations produced a hole 0.9 cm in diameter. Both calculations show that hole growth ceases by 20 µs. The empirical model (Ref. 8) predicted a hole diameter of 1.20 cm. Experimental hole size could not be determined from the photographs. Because SPH calculated a larger hole size in the shield, one can assume that more mass was transferred to the resulting debris cloud in XH-9.

One prominent difference between the CTH and the SPH calculations for XH-9 was the time at which the debris cloud first impacted the witness plates. The CTH code calculated that the witness plate was impacted at 12.5 µs while SPH calculated an impact time of 14.5 µs. In the experiment, the witness plate was estimated to be hit at 10.4 µs.

A second difference in the XH-9 calculations was in the dynamics of the debris clouds. The CTH code calculated a debris cloud with an axial velocity of 11.9 km/s and a radial velocity of 5.9 km/s. The SPH code calculated a slower debris cloud with an axial velocity of 10.5 km/s and a radial velocity of 4.25 km/s. The experimental debris cloud was estimated from the pulsed laser photographs to have an axial velocity of 14.65 km/s and a radial velocity of 8.34 km/s.

Witness plate damage was another area for which the codes had different results. The SPH code calculated the damage to the witness plate in XH-9 to be more extensive than that calculated by CTH. At 21 µs, SPH predicted that the most damage would occur slightly away from the center of the witness plate (at tracer 9). Here the witness plate received a velocity of 354 m/s and a displacement of 0.134 cm. The CTH code calculated that material in the plate closest to its center (tracer 7) received a velocity of 170 m/s and a displacement of 0.07 cm. It is not possible to make any substantive conclusions regarding the witness plate damage from the experimental pulsed laser photographs.

Since the CTH calculation of XH-10 was only carried out to 10 µs, only the hole size and debris cloud dynamics can be used in a direct comparison to the calculation and the experimental results.

At 10 μs the hole produced in the stand-off shield in the CTH calculation of XH-10 is 0.99 cm while the SPH calculation produced a hole diameter of 0.92 cm. Kinslow's empirical model predicted a value of 1.22 cm for hole diameter.

The SPH code calculated that the witness plate of XH-10 was impacted at 14.4 μs. In the XH-10 experiment, the witness plate was estimated to be hit at 9.8 μs.

The debris cloud calculated by CTH for XH-10 travels axially and expands radially at a faster rate than that calculated by SPH. The CTH code calculated a debris cloud with an average axial velocity of 12.2 km/s and an average radial velocity of 6.16 km/s. The SPH code calculated a debris cloud with an average axial velocity of 10.7 km/s and an average radial velocity of 4.35 km/s. The experimental debris cloud was estimated from the high-speed photographs to have an axial velocity of 15.56 km/s and a radial velocity of 8.16 km/s.

For the XH-10 calculation, SPH predicted that the material in the witness plate closest to its center (tracer 7) received a velocity of 359 m/s and a displacement of 0.136 cm. It is not possible to make any substantive conclusions regarding the witness plate damage from the experiment.

6.3 EXPERIMENTS WS-11 AND WS-12

6.3.1 Description of Experiments WS-11 and WS-12

The objective of the WS-11 and WS-12 experiments was to find an optimum Whipple bumper shield configuration for protection against projectiles traveling in excess of 10 km/s. References 4, 10, and 11 describe the experiments and corresponding CTH calculations. These CTH calculations are now reproduced in this study using updated constants for the ANEOS. Also, the cell size was held constant throughout the computational mesh to avoid numerical problems associated with neighboring cells of dissimilar size or nonsquare cells. The WS-11 and WS-12 experiments were similar in material type and stand-off shield and witness plate thicknesses. There was a large difference in the initial energy of the tests. The WS-12 test had almost twice the kinetic energy of WS-11 due mainly to differences in the initial projectile mass (see Table 1). Experiment WS-11 had an initial kinetic energy of 17.5 kJ while WS-12 had 33.3 kJ. Two sets of high-speed photographic data are available for the WS-11 and WS-12 experiments. The first set offers side views of the propagation of the debris cloud up to the point where it hits the witness plate (Figs. 24 and 25). The second set offers views of the back of the witness plate and its response from the impacting debris cloud (Figs. 26 and 27). During the time that the back

31

8.7 μs   4.7 μs   0.7 μs

10.7 μs   6.7 μs   2.7 μs
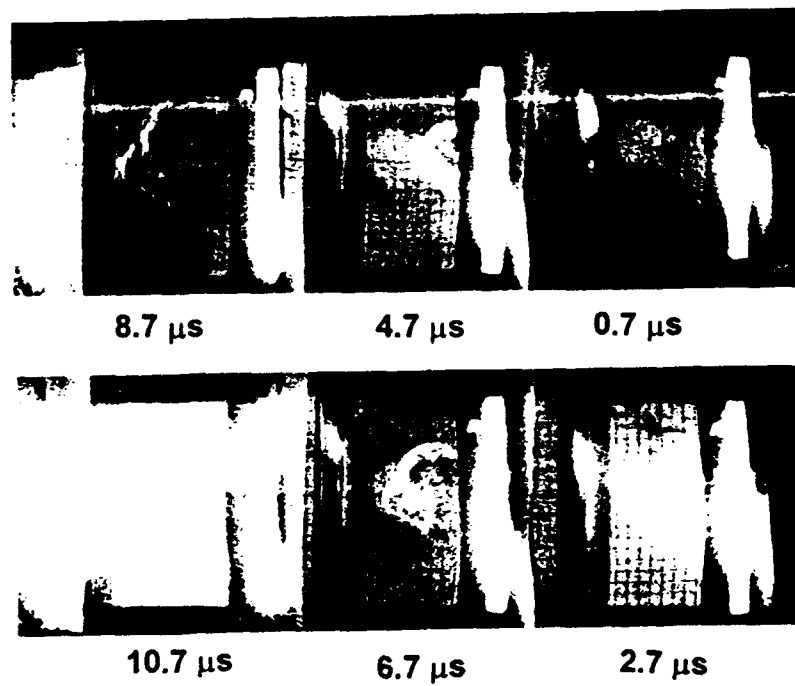
Figure 24. Experiment WS-11, side view.

8 μs   6 μs   4 μs   2 μs   0 μs

9 μs   7 μs   5 μs   3 μs   1 μs
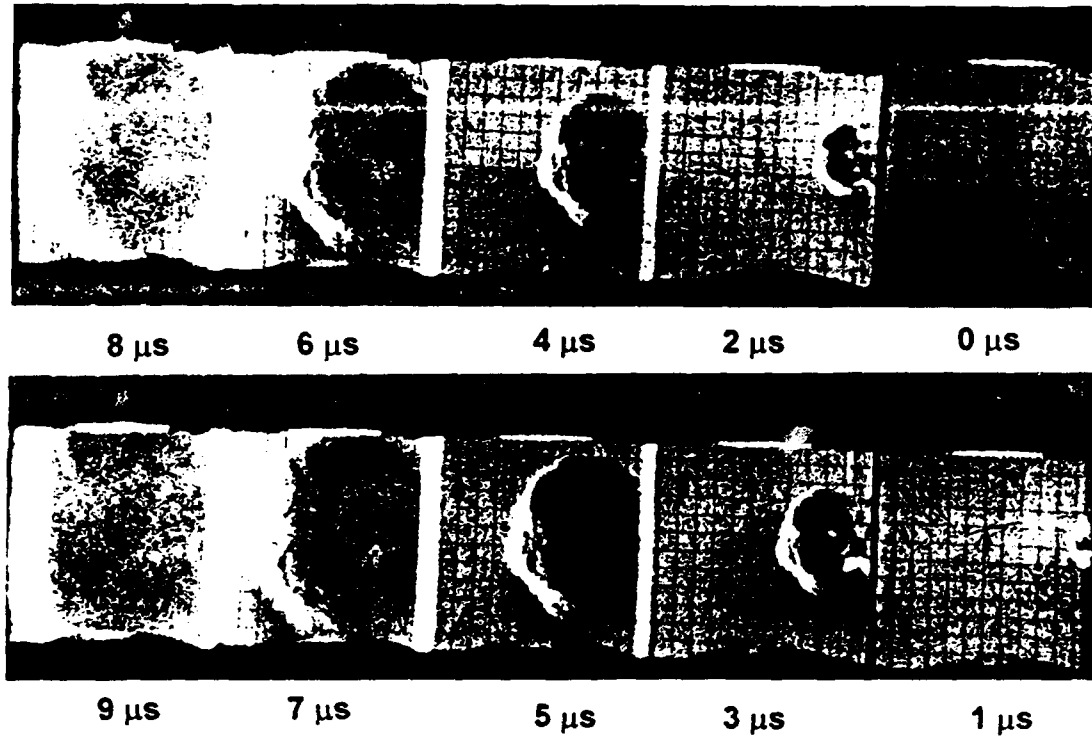
Figure 25. Experiment WS-12, side view.

54.7 µs   44.7 µs   34.7 µs   24.7 µs   14.7 µs

59.7 µs   49.7 µs   39.7 µs   29.7 µs   19.7 µs
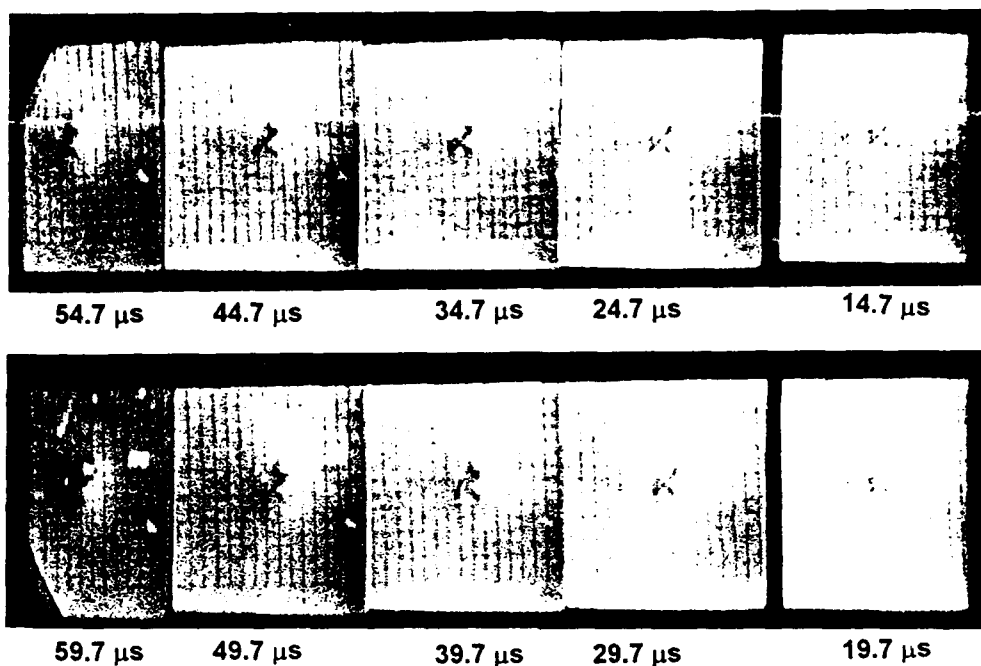
Figure 26. Experiment WS-11, back surface view.

48 µs   38 µs   28 µs   18 µs   8 µs

53 µs   43 µs   33 µs   23 µs   13 µs

Figure 27. Experiment WS-12, back surface view.

33

of the witness plates were photographed (out to about 60 µs), WS-12 showed perforation while WS-11 did not. Due to the nature of the experiments, the witness plates were not recovered; thus damages occurring at later times could not be assessed.

Individual pieces of existing orbital debris which may impact a spacecraft will usually be roughly plate- or disk-shaped. A "flat-on" impact of this type of debris may produce more damage than an equivalent compact mass. It has been numerically shown here and in Reference 4 that equivalent mass p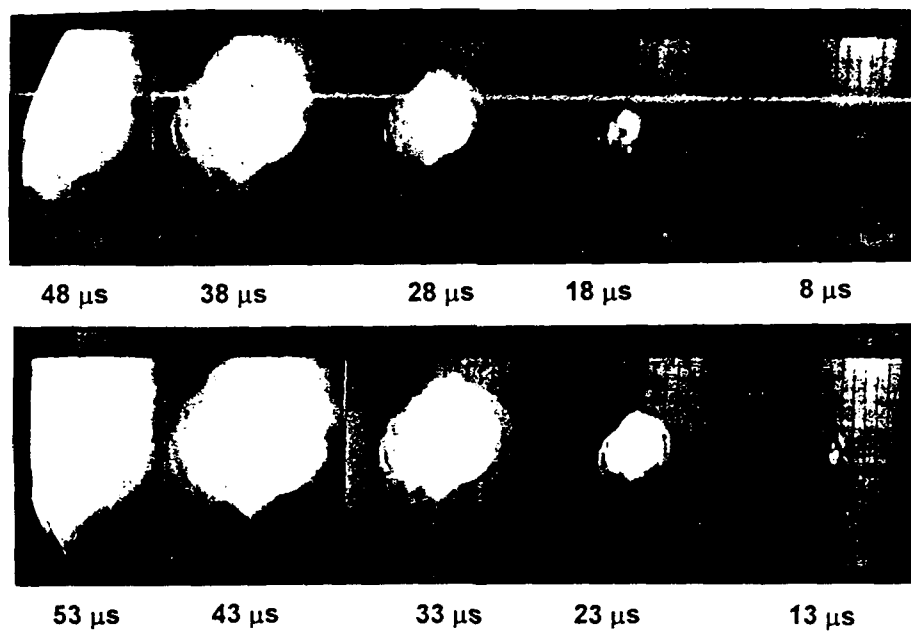rojectiles with different shapes (sphere versus plate) will affect the extent of damage to the witness plate. The flyer plate projectile produces a debris cloud with a smaller divergence angle than that of a spherical projectile. Because of this, the mass and energy of the debris cloud are concentrated over a smaller area on the witness plate resulting in more damage.

The experiments for WS-11 and WS-12 used a disk-shaped projectile (flyer plate). The numerical simulation for these experiments was carried out using a representation of both a sphere- and disk-shaped projectile of equivalent mass. The 2-D calculations that used disk-shaped projectiles did not match the irregularities and distortions often observed in the experimental flyer plate prior to impact. The effect of these irregularities and distortions can be observed in the XH-9 and XH-10 experiments described in Subsection 6.2.

6.3.2 CTH Results for WS-11 and WS-12 -- Sphere

The shape of the debris cloud in the WS-11 simulation prior to impact with the witness plate is shown in Figure 28. The axial velocity at 10 µs is about the same as that of the debris cloud in WS-12. Experiment WS-11 had about 47 percent less initial kinetic energy than WS-12. This difference resulted in perforation of the witness plate in the WS-12 experiment but no perforation was seen in the WS-11 experiment during the time span of the photographs (54.7 µs) (Ref. 4). The CTH calculations matched these results numerically up to 20 µs although a disk-shaped projectile (used in Subsection 6.3.3) is a more accurate simulation of the experiment. The debris cloud in the WS-11 calculation had axial and radial velocities of 9.5 and 3.6 km/s, respectively. Impact of the witness plate occurs at 11.5 µs for both simulations. The material and density plots for WS-11 at 20 µs, shown in Figure 29, show that the debris cloud has not perforated the witness plate at this time. Peak velocity for WS-11 near the center of symmetry (tracer 7) is about 140 m/s compared to 300 m/s for WS-12 at tracer 7.

Material model, equation of state, and cell size were identical for both WS-11 and WS-12 calculations. Cell size was kept constant at 0.03175 cm over the entire mesh for both calculations. This size resulted in four cells across the thinnest dimension for each calculation.

Experimental results of WS-12 show definite perforation of the witness plate by about 13 µs (Ref. 4). The CTH calculation shows perforation occurring at 20 µs (Fig. 30). The larger mass in the projectile of the WS-12 calculation produces a debris cloud with a kinetic energy of about 25.0 kJ which was 13 kJ more energetic than the debris cloud calculated in WS-11. Average radial and axial velocities of the debris cloud were 9.7 and 4.4 km/s, respectively. Impact of the witness plate by the debris cloud was calculated to occur at about 11.75 µs.

The CTH calculations revealed that the Lagrangian tracer located 0.375 cm from the center of the witness plate in the WS-12 calculation was traveling at a velocity that was over two times that of the WS-11 calculation at 20 µs (Fig. 31). The WS-12 calculation showed that the witness plate had suffered 65-percent penetration (distance through the witness plate) while the WS-11 calculation showed 37-percent penetration at 17 µs. At 20 µs the witness plate in WS-12 was perforated while the witness plate in WS-11 was about 67-percent penetrated. Displacement of the witness plate at tracers 7, 9, and 11 is shown in Figure 32.

Maximum shear stress in the witness plate reached a peak value of 200 MPa for both the WS-11 and WS-12 calculations (Fig. 33). Debris cloud divergence angles for WS-11 and WS-12 were both 80 deg.
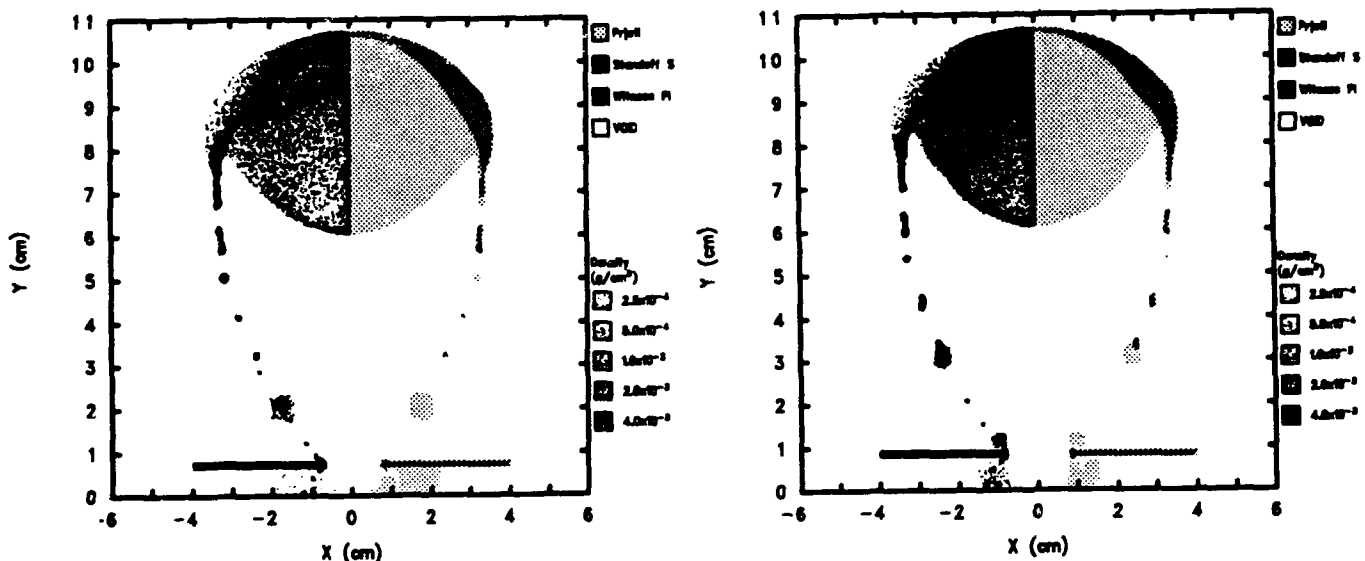

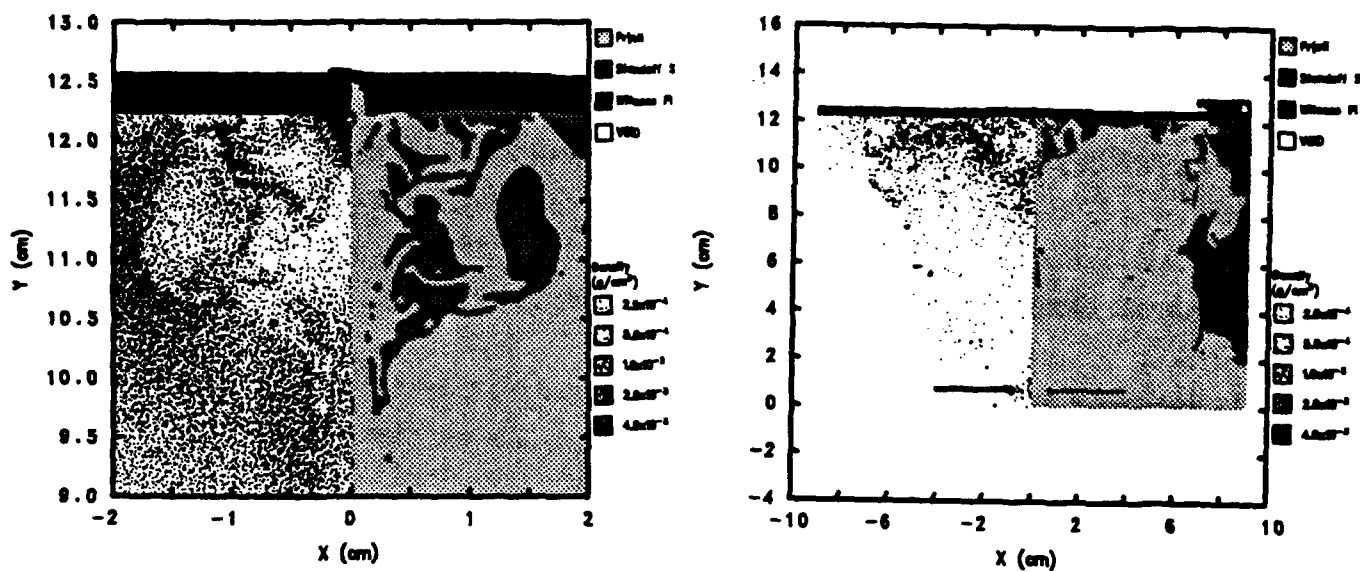Figure 28. CTH material plots of WS-11 and WS-12 at 10 µs (sphere).

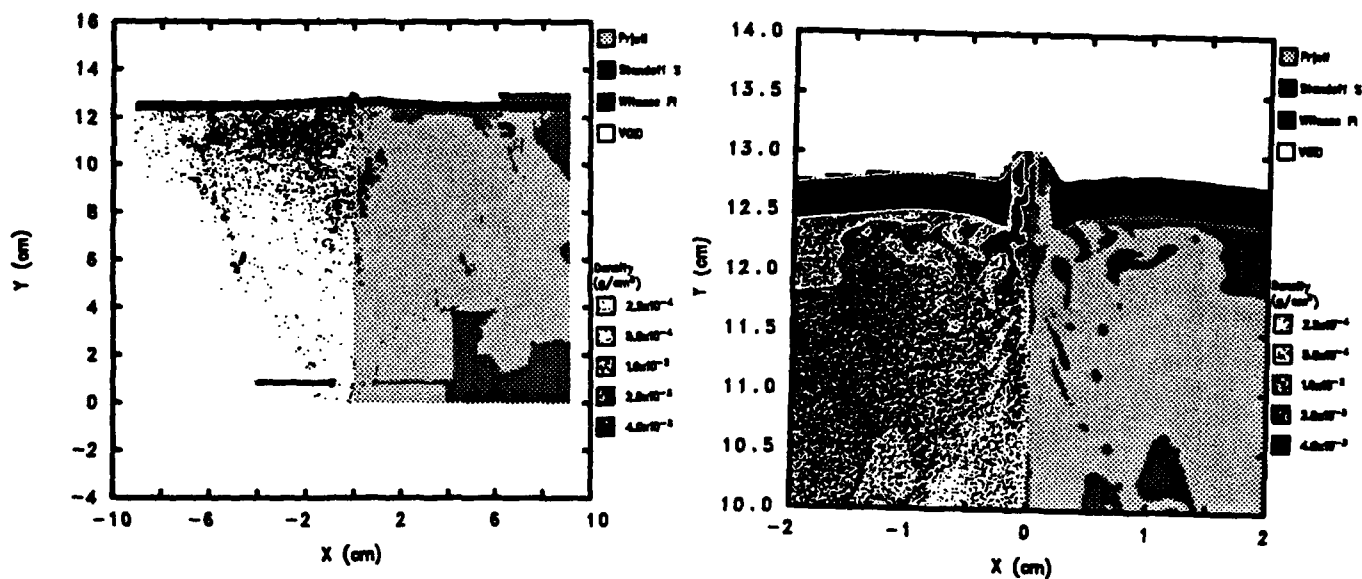Figure 29. CTH material plots of WS-11 at 20 µs (sphere).

Figure 30. CTH material plots of WS-12 at 20 µs (sphere).
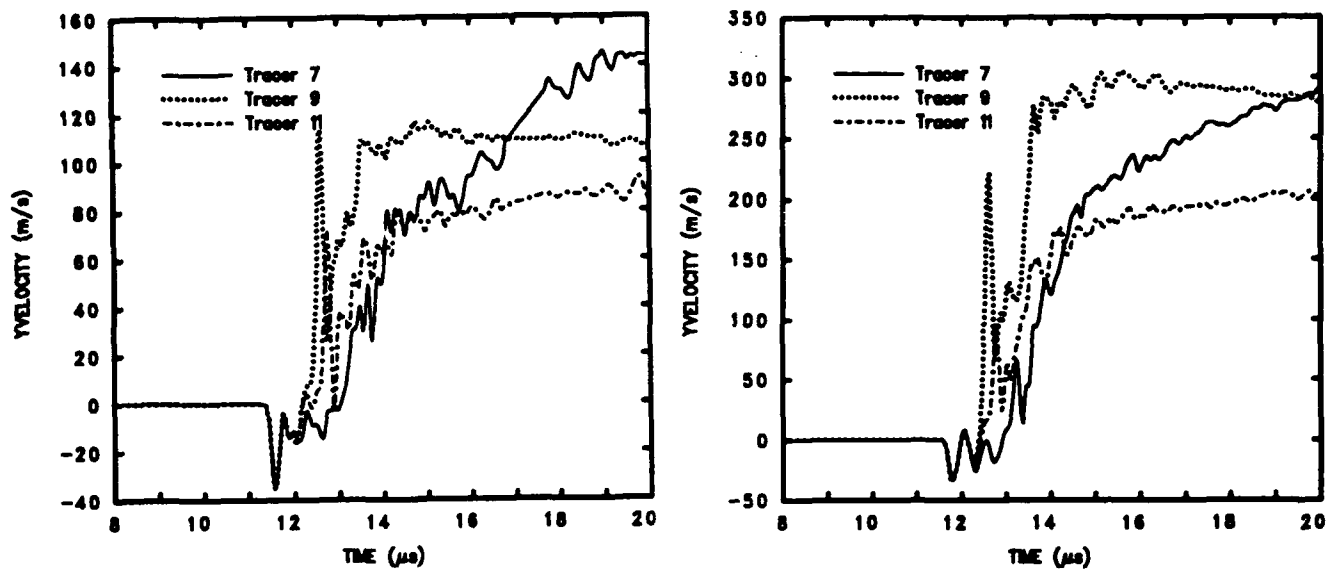
36

Figure 31. CTH y-velocity plots of WS-11 and WS-12 (sphere).
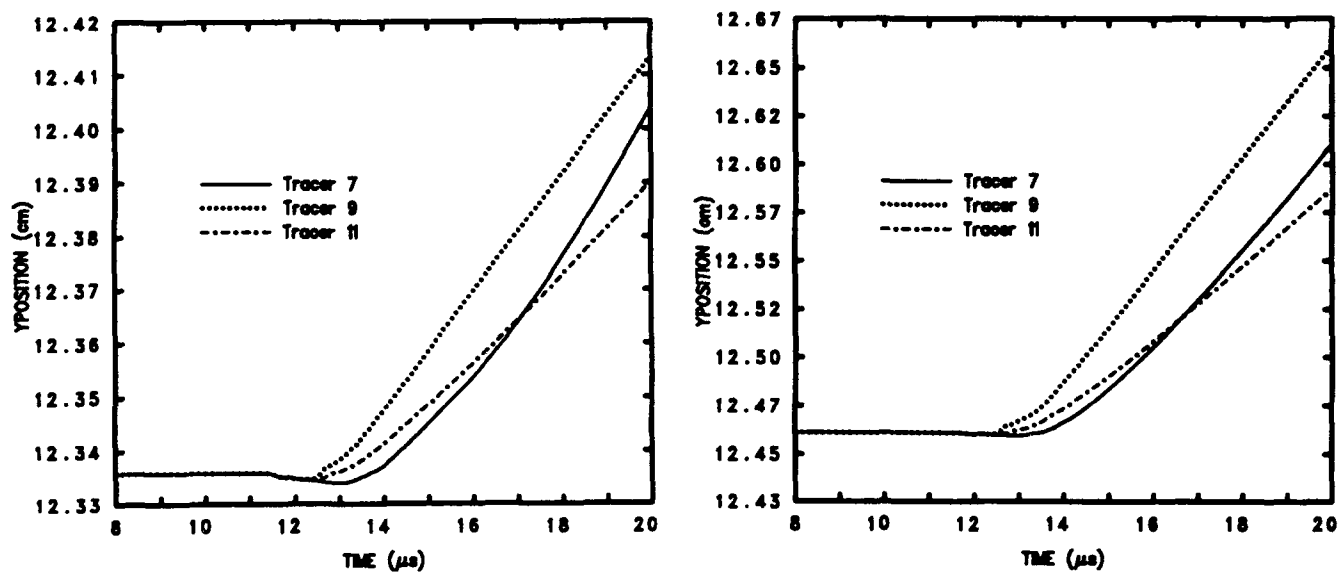

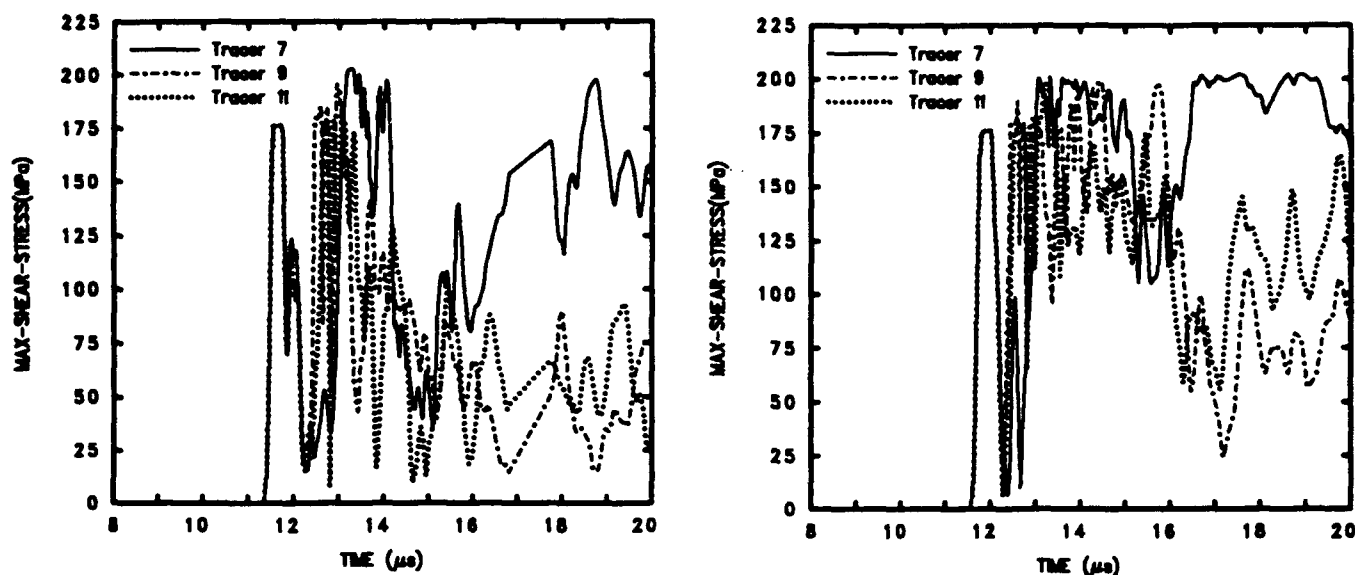Figure 32. CTH y-displacement plots of WS-11 and WS-12 (sphere).

Figure 33. CTH maximum shear stress plots of WS-11 and WS-12 (sphere).

6.3.3 CTH Results for WS-11 and WS-12 -- Flyer Plate

The nature of these flyer plate problems resulted in an extremely small time step about 6 μs after interaction of the projectile with the witness plate. Time step problems were also observed in calculations described in Subsection 6.3.4.

The shape of the debris cloud in the WS-11 simulation at 10 μs (prior to impact with the witness plate) is shown in Figure 34. The effect of projectile shape can be seen in the narrow shape of the debris cloud compared to that resulting from a spherical projectile (Fig. 28). The calculation of WS-11 was carried out to 21 μs. Material and density plots of WS-11 at 16 and 21 μs are shown in Figures 35 and 36. Complete perforation occurred at a calculated time of 21 μs. The extent of penetration and damage is qualitatively similar for both calculations up to 16 μs. After 16 μs, the witness plate in the WS-11 calculation is damaged sooner than the one in the WS-12 calculation (Fig. 36). Complete perforation occurs at 21 μs for WS-11 and at 23 μs for WS-12.

Although the WS-12 calculation had about twice the initial kinetic energy of WS-11, the diameter of the flyer plate in WS-11 was 50 percent less than the one in WS-12. The smaller area of impact on the witness plate in WS-11 may have offset the damaging effects of increased kinetic energy in WS-12. More of the kinetic energy in WS-12 was transmitted to tracers 9 and 11 (compare the velocities at tracers 9 and 11 in Fig. 37).

38
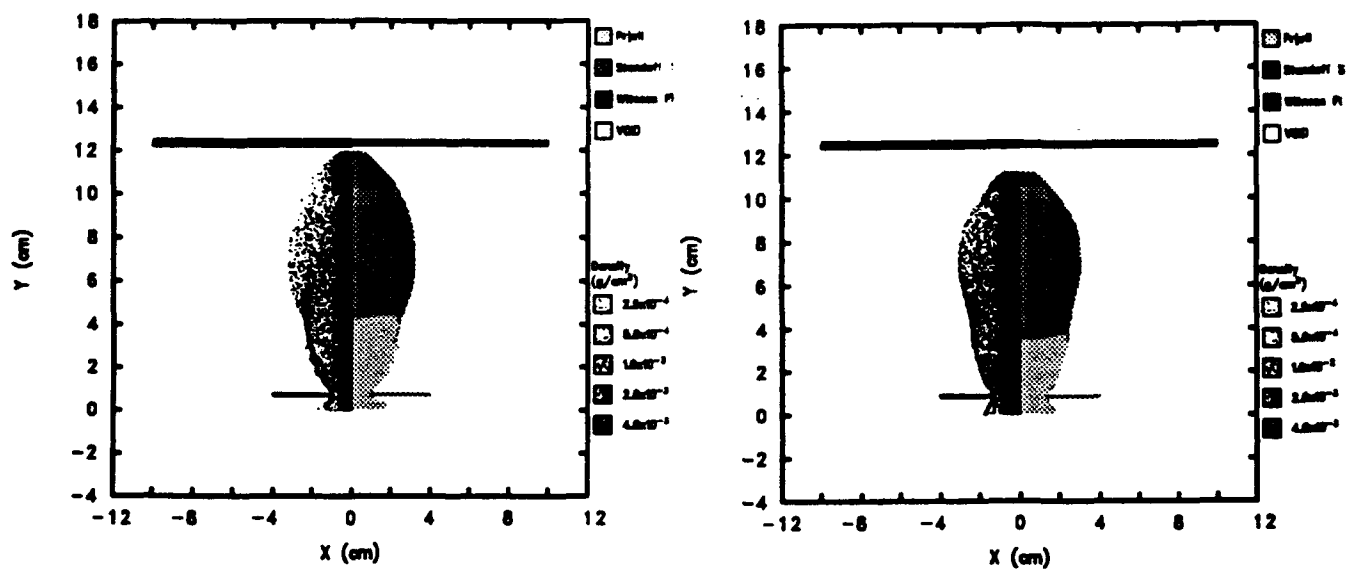
Figure 34. CTH material plots of WS-11 and WS-12 at 10 µs (disk).
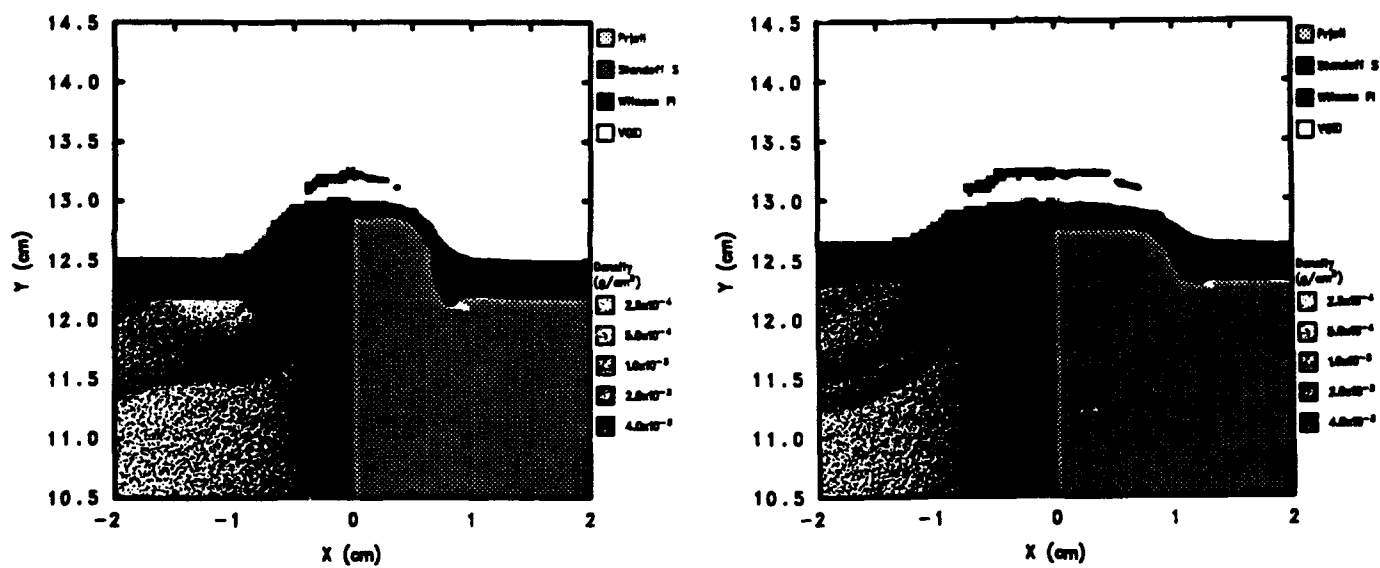
Figure 35. CTH material plots of WS-11 (left) and WS-12 (right) at 16 µs (disk).

39
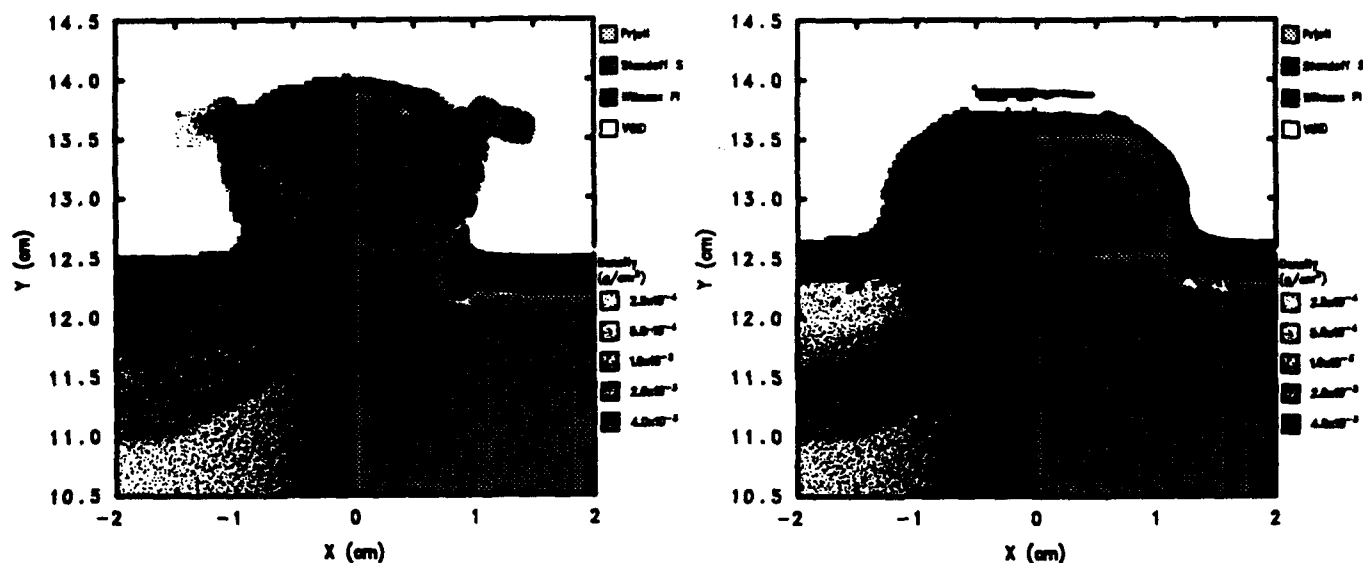
Figure 36. CTH material plots of WS-11 and WS-12 at 21 µs (disk).
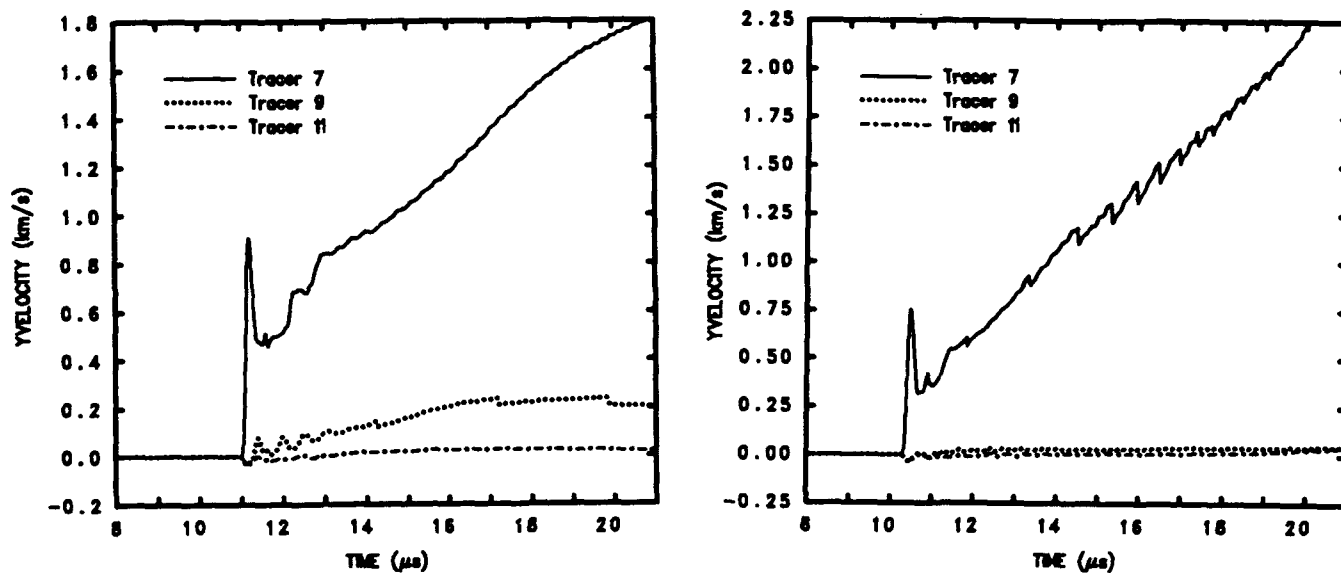
Figure 37. CTH y-velocity plots of WS-11 and WS-12 (disk).

This high density jet along the axis of the debris cloud is responsible for the greater extent of damage than that produced by a debris cloud from a spherical projectile. The effect on the witness plate produced by the two kinds of clouds can be seen by comparing the velocity plots of points on the witness plate for spherical and disk-shaped projectiles (Figs. 31 and 37). Tracer 7

(closest to the axis) receives most of the velocity in Figure 37 while the velocity is approximately evenly distributed among the three tracers (7, 9, and 11) for the calculation using a spherical projectile (Fig. 31). Displacement of the center of the witness plate (tracer 7) relative to the outer edge (tracers 9 and 11) is also greater for the disk-shaped projectile than for spherical projectile (Figs. 32 and 38).

The debris cloud in the WS-11 calculation had axial and radial velocities of 11.28 and 3.2 km/s. The axial velocity was considerably higher for a disk than a sphere (9.5 km/s versus 11.28 km/s). The radial velocities were similar for both spherical and disk projectiles. Impact of the witness plate was calculated to be 10.28 µs for the calculation using disk-shaped projectiles.

Material and density plots of the WS-12 disk calculation at 10, 16, and 21 µs are shown in Figures 34-36. The CTH calculation using a plate showed perforation of the WS-12 witness plate to occur at 23 µs. Experimental results of WS-12 show perforation of the witness plate by about 13 µs. Axial and radial velocities of the debris cloud in the WS-12 CTH calculation were 10.2 and 3.5 km/s, respectively. Impact of the witness plate occurred at 11.2 µs.

At 16 µs, the disk projectile penetrated 38 percent of the witness plate in WS-12 (63% penetration in WS-11). A perforation of 38 percent in the witness plate of WS-12 corresponds to a back surface bulge of about 3 mm. Experimental photographs show approximately a 15-mm bulge just prior to rupture. The Calculation shows about 11 mm of bulge prior to rupture

Maximum shear stress was plotted for the witness plate in the disk calculations for WS-11 and WS-12 (Fig. 39). Maximum shear stress in the witness plate reached a peak value of 200 MPa for both the WS-11 and WS-12 calculations. Velocity in the y-direction as monitored by tracers 7, 9, and 11 is shown in Figure 37. This figure shows that the witness plate was impacted at about 10.3 µs (WS-11) and 11.2 µs (WS-12). Debris cloud divergence angles for WS-11 and WS-12 were both about 12 deg.

Figure 38. CTH y-displacement plots of WS-11 and WS-12.
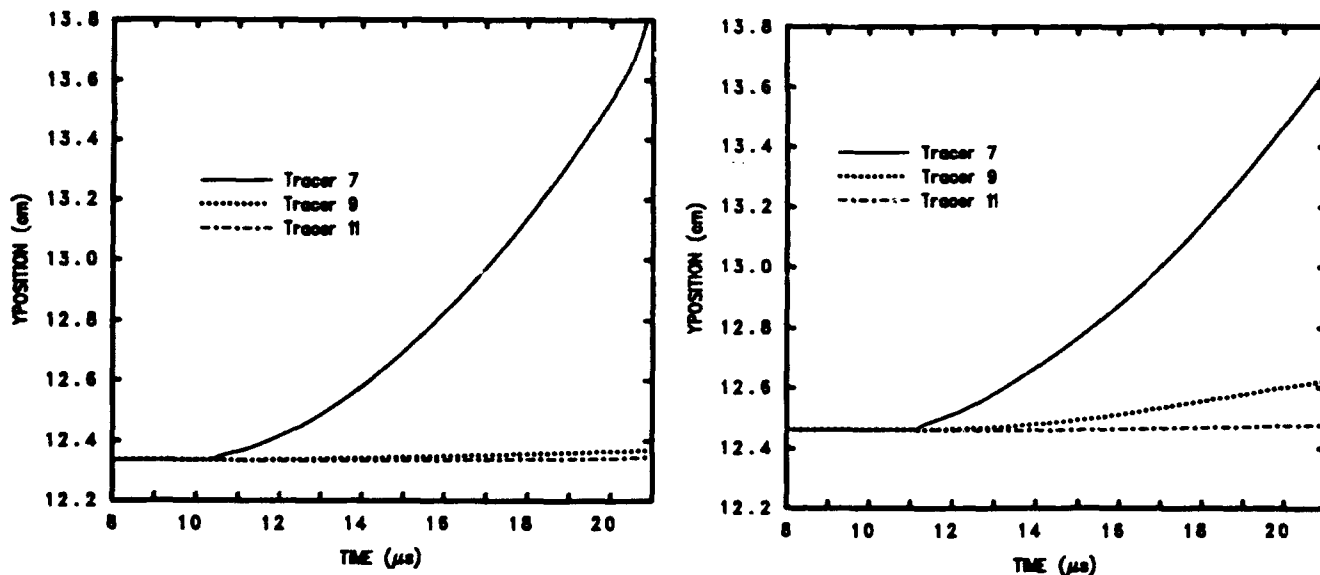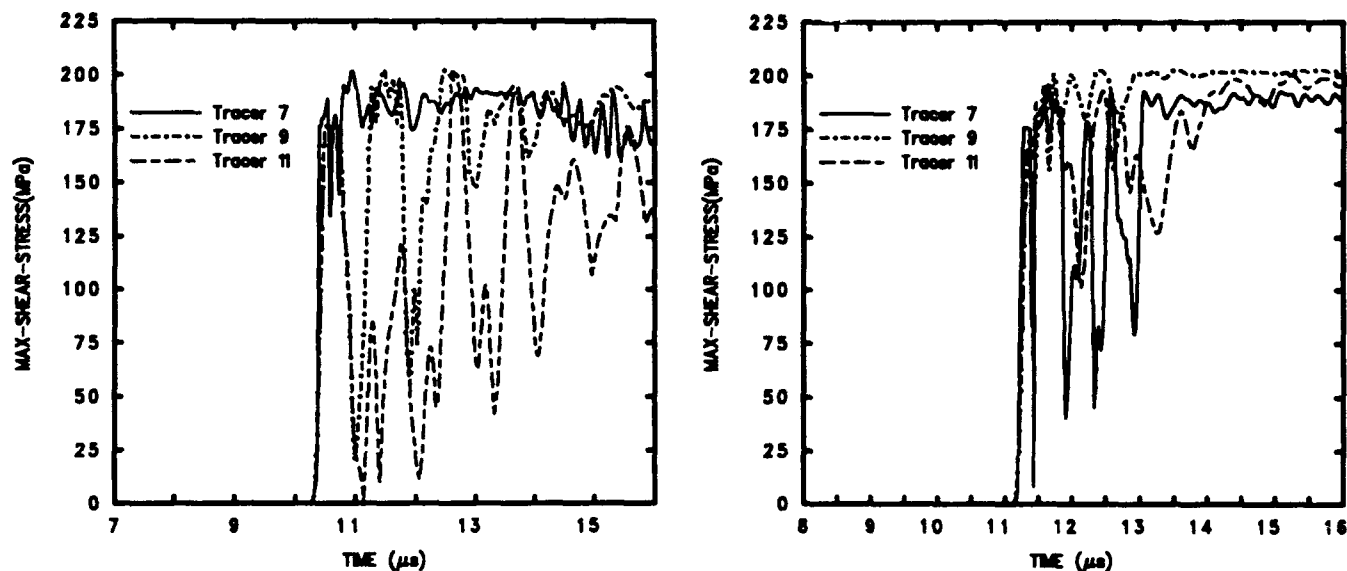

Figure 39. CTH maximum shear stress plots of WS-11 and WS-12 (disk).

6.3.4 SPH Results for WS-11 and WS-12 -- Sphere

To allow for witness plate deformation, the input files for problems WS-11 and WS-12 were modified to include a longer witness plate and larger problem dimension. The SPH results have been compared to the experimental data for WS-11 and WS-12.

42

With a spherical projectile, debris cloud in the WS-11 calculation did not expand as rapidly in the axial direction as the WS-11 experimental debris cloud and consequently took slightly longer to hit the witness plate. The experimental debris cloud hit the WS-11 witness plate at about 8.7 μs. The SPH cloud in the WS-11 calculation hit the witness plate at 11.2 μs. The debris cloud seen in the experiment was determined to have an axial velocity of over 13.1 km/s and a radial velocity of over 7.0 km/s. The SPH calculation produced a debris cloud with an axial velocity of 10.2 km/s and a radial velocity of 4.1 km/s. Experimental results show some witness plate deformation but no rupture prior to 60 μs. Figure 40 shows that SPH calculates a similar result (note that plots shown in Figure 40 correspond in time with the experimental photographs). At 60 μs, the witness plate has a 4.2-cm bulge. This bulge is moving at 0.5 km/s and would rupture if the calculation were carried out further. Debris cloud and ejecta divergence angles converged to values of 78 and 74 deg, respectively, for the WS-11 calculation.

Again, axial expansion was slower in the WS-12 calculation using a spherical projectile compared to the experiment results. The experimental cloud in WS-12 expanded axially at 14.1 km/s and radially at 7.3 km/s. The SPH debris cloud had a leading edge velocity of 10.1 km/s and a radial velocity of about 4.4 km/s. Witness plate impact occurs at 11.4 μs for the WS-12 calculation and at 8 μs for the WS-12 experiment. Figure 41 shows material plots at times that correspond to the WS-12 side view photographs. The SPH code predicts damage to the witness plate that is qualitatively similar to the experimental damage. Figure 42 shows the emergence of a secondary debris cloud for SPH calculation.

Cloud and ejecta divergence angles converged to values of 80 and 76 deg, respectively, for the WS-12 calculation. These values are slightly larger than divergence angles for WS-11 due to the increased initial projectile energy in WS-12.

The difference in the initial kinetic energy of the WS-11 and WS-12 calculations resulted in differing levels of damage to the witness plate. This is evident in Figure 43 which shows a close-up view of the debris cloud, witness plate interaction at 17 μs, and Figure 44 which shows SPH material plots at 60 μs for both the WS-11 and WS-12 calculations. These figures show that the WS-12 calculation has received a deformation to the witness plate that considerably exceeds the deformation calculated for WS-11. A secondary debris cloud has formed and propagates away from the back surface of the witness plate in the WS-12 calculation. The bulge in the witness plate for the WS-11 calculation at 60 μs is displaced by 3.8 cm and is moving at a velocity 360 m/s. The WS-12 calculation at 60 μs shows a hole in the witness plate through which projectile

43

material is moving. At this time the secondary debris cloud is 28 cm long in the y-direction and the material at the leading edge is moving at 5.95 km/s.
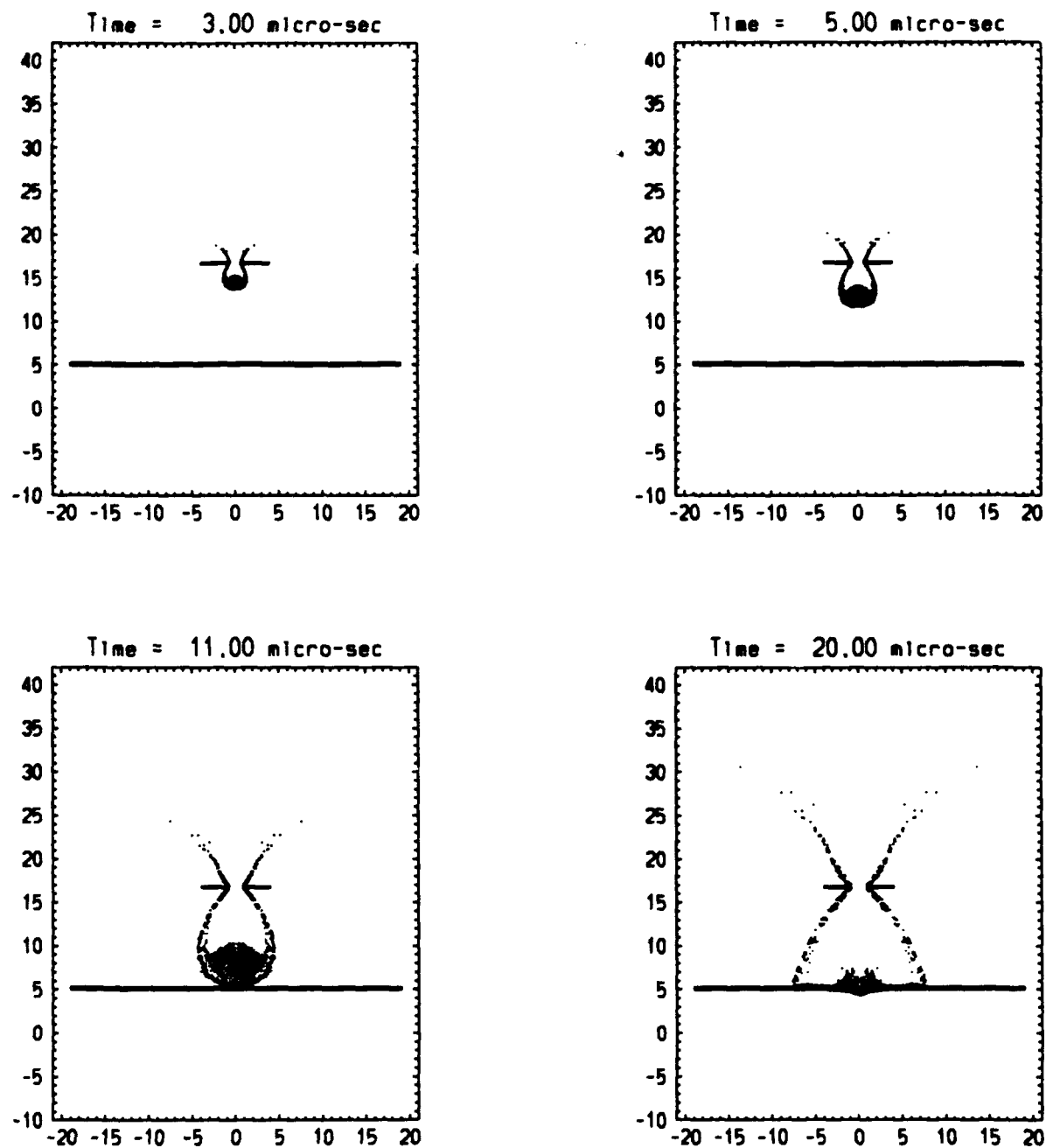
Figure 40. SPH material plots corresponding to WS-11 photographic times.

44

Displacement and velocity in the *y*-direction and xy stress were plotted as a function of time for the SPH WS-11 calculation. These plots are presented in Figures 45-46. The figures demonstrate that the debris cloud hits the witness plate at just over 11 μs for both calculations. Figure 44 (right) shows that the witness plate for the WS-12 calculation has received more kinetic energy than the witness plate in the WS-11 calculation.
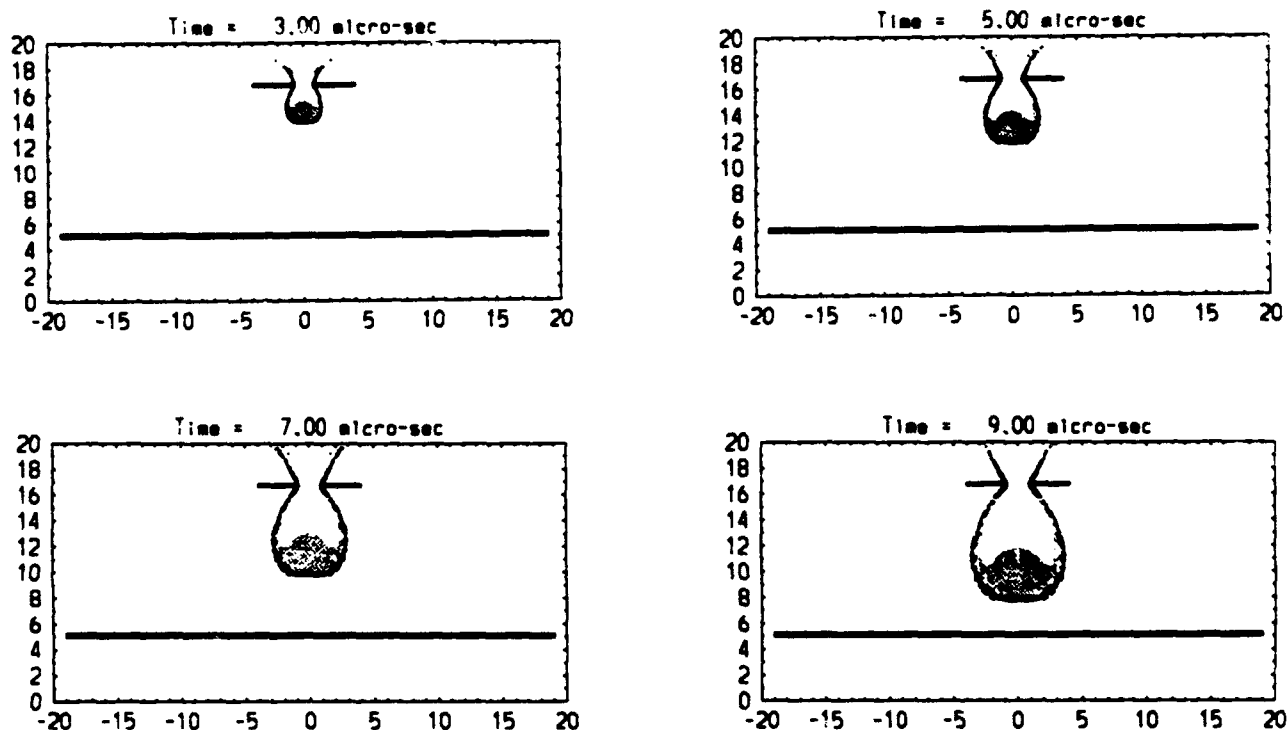
Figure 41. SPH material plots corresponding to WS-12 side view photographs (sphere).
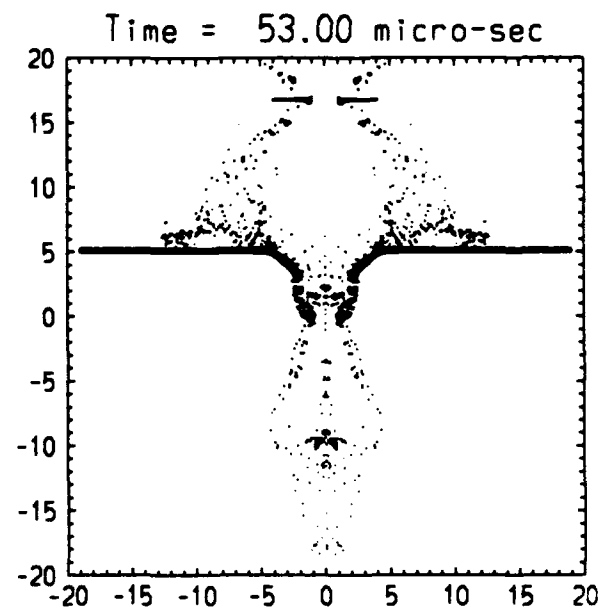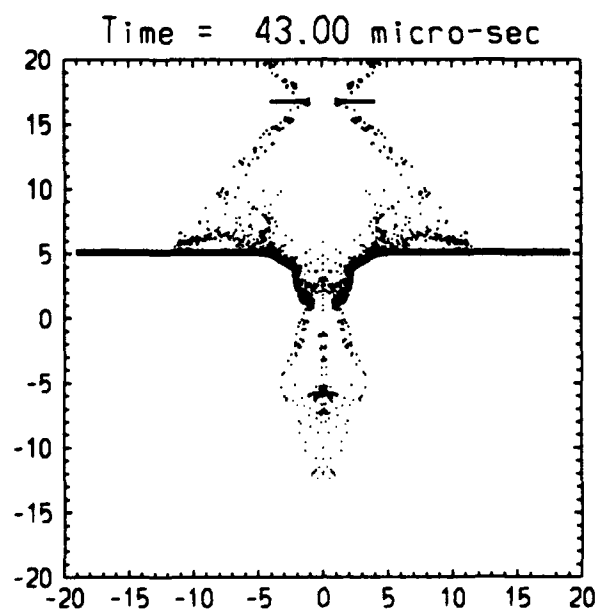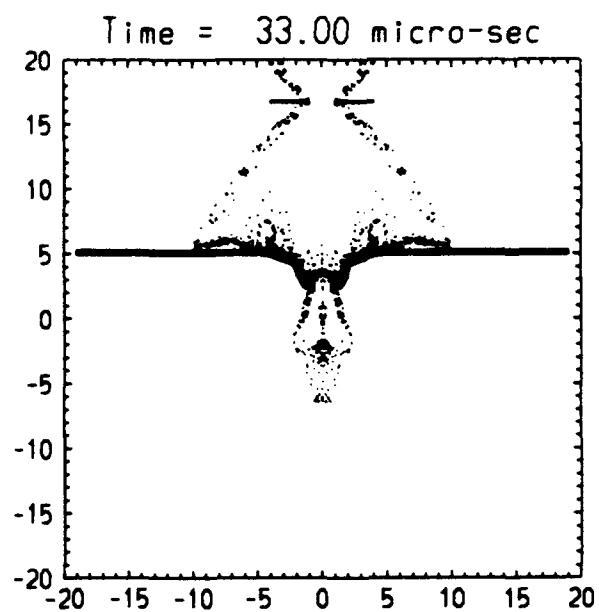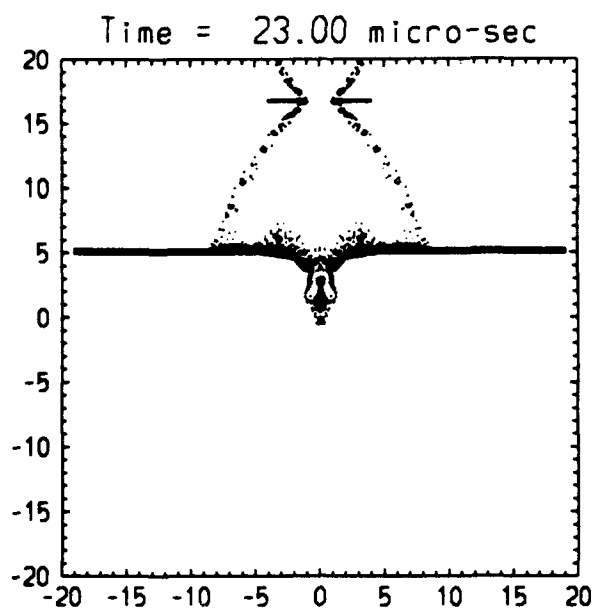
Figure 42. SPH material plots corresponding to WS-12 back surface photographs (sphere).

46
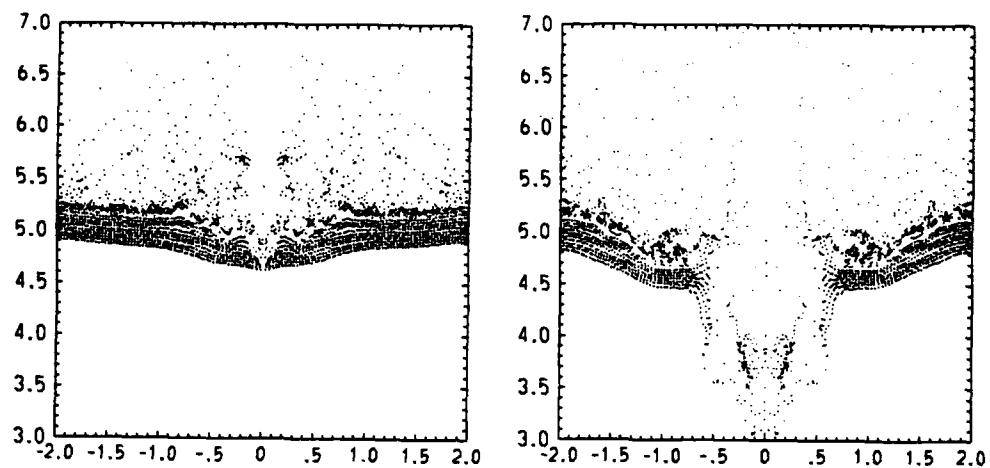
Figure 43. SPH material plots of WS-11 (left) and WS-12 (right) at 17 μs (sphere).
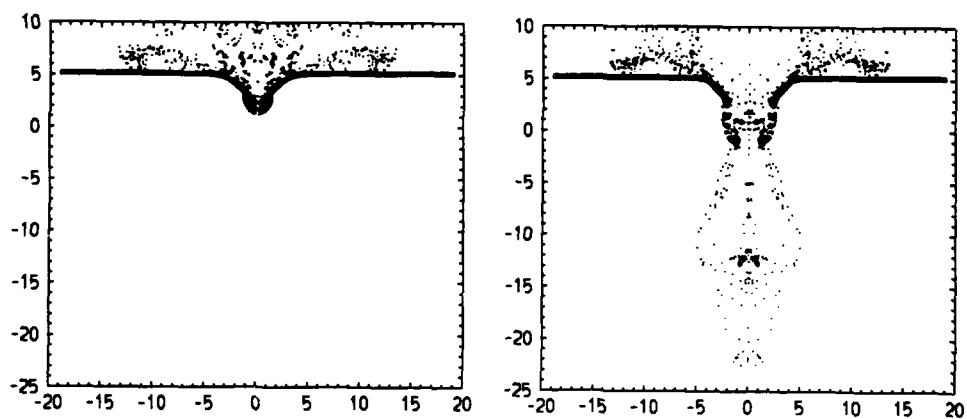
Figure 44. SPH material plots of WS-11 (left) and WS-12 (right) at 60 μs (sphere).

47
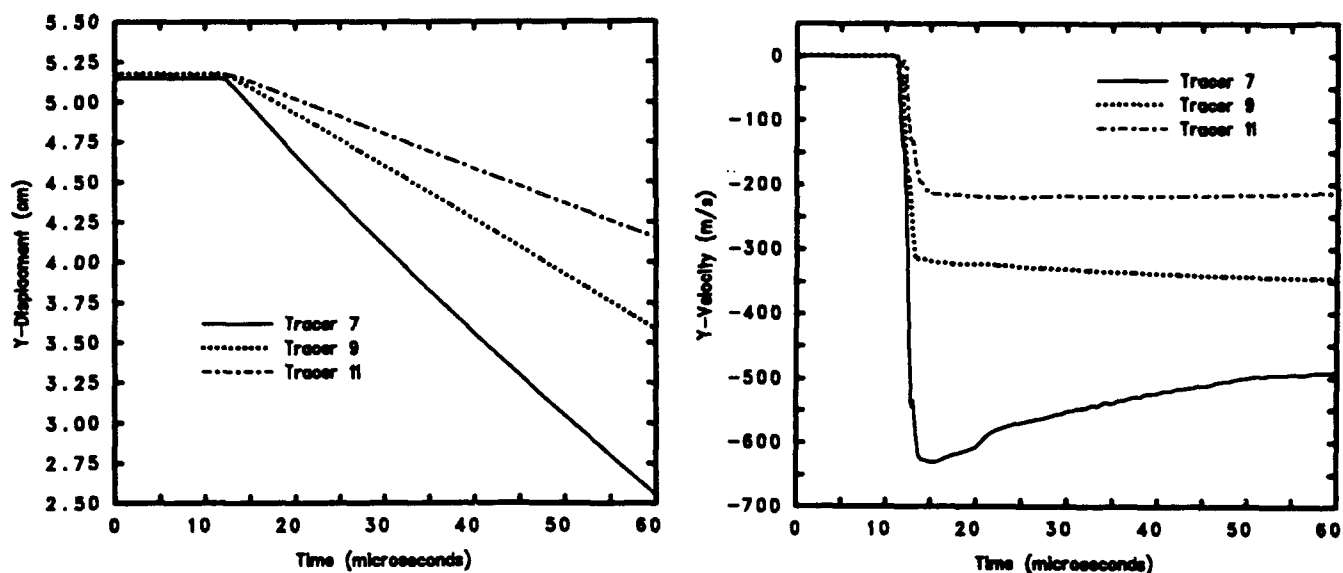
Figure 45. SPH *y*-displacement and *y*-velocity plots of WS-11 (sphere).
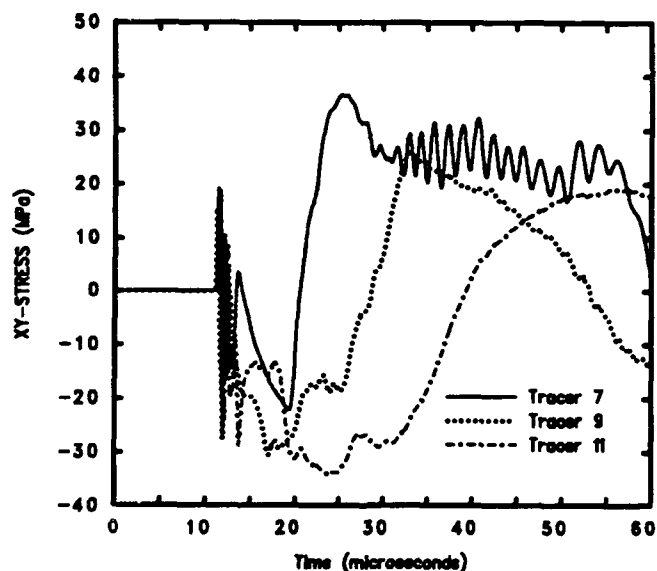
Figure 46. SPH xy stress plot of WS-11 (sphere).

6.3.5 SPH Results for WS-11 and WS-12 -- Flyer Plate

Like CTH, the nature of this problem led to numerical problems about 5 μs after impact with the witness plate. In CTH, the time step became too small. In SPH, creation of "hot particles" occurred within the impact area which led to an excessively small time step. These "hot particles"

48

are particles with unrealistically high or low values of density and energy. These were manually removed until the solution was overly affected. The results of the calculations were acceptable up to about 5 μs after impact.

Material plots of the WS-11 calculation corresponding to photographic times (Fig. 24) are shown in Figure 47. The SPH debris cloud propagated at nearly the same speed as the experimental debris cloud and impacted the witness plate at about the same time. The experimental debris cloud hit the witness plate at about 8.7 μs. The SPH cloud formed by a disk-shaped projectile hit the witness plate at 9.1 μs. Axial velocity was also very close to the axial velocity seen in the experiment (see Table 6). Experimental results show some witness plate deformation but no rupture prior to 60 μs. The calculation using a flyer plate reached a time of 14 μs at which time the damage to the witness plate (Fig. 48, left) seems to have been affected by "hot particle" removal as seen in the unphysical deformation of the witness plate along the axis of symmetry. However, it is possible to deduce that overall damage was predicted to be more severe for the witness plate of WS-11 than that of WS-12. The CTH code also predicted a more severe damage pattern for the witness plate of WS-11 than that of WS-12.

Debris cloud and ejecta divergence angles converged to values of 66 and 54 deg, respectively, for the WS-11 calculation using a flyer plate.
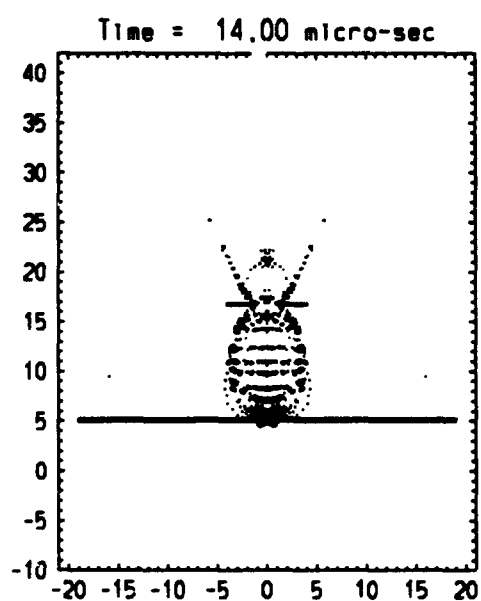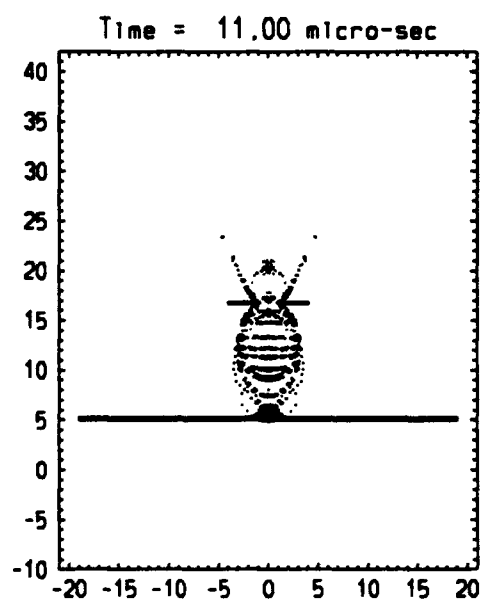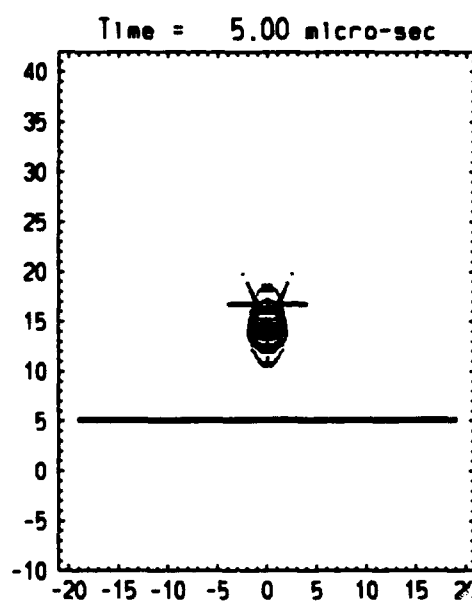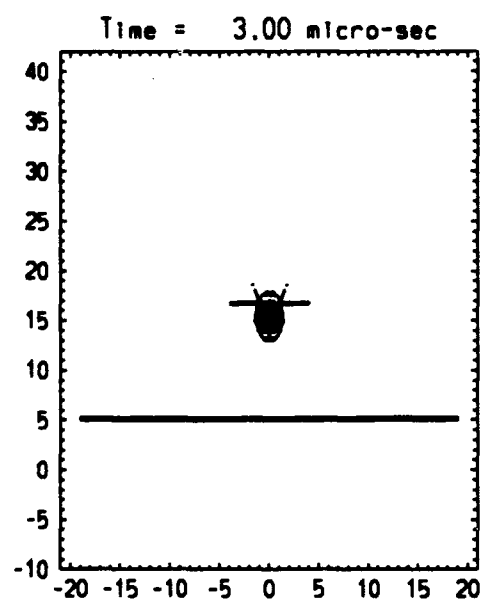
Figure 47. SPH material plots corresponding to WS-11 photographic times (disk).

Table 6. Debris cloud radial and axial velocities, WS-11 and WS-12.

	WS-11 sphere/plate		WS-12 sphere/plate	
	Axial Velocity, km/s	Radial Velocity, km/s	Axial Velocity, km/s	Radial Velocity, km/s
CTH	9.5/11.28	3.6/3.2	9.7/10.2	4.4/3.5
SPH	10.2/12.5	4.1/3.4	10.1/11.2	4.4/3.8
Experiment	a/13.1	a/7.0	a/14.1	a/7.3

a Experiments used flyer plates
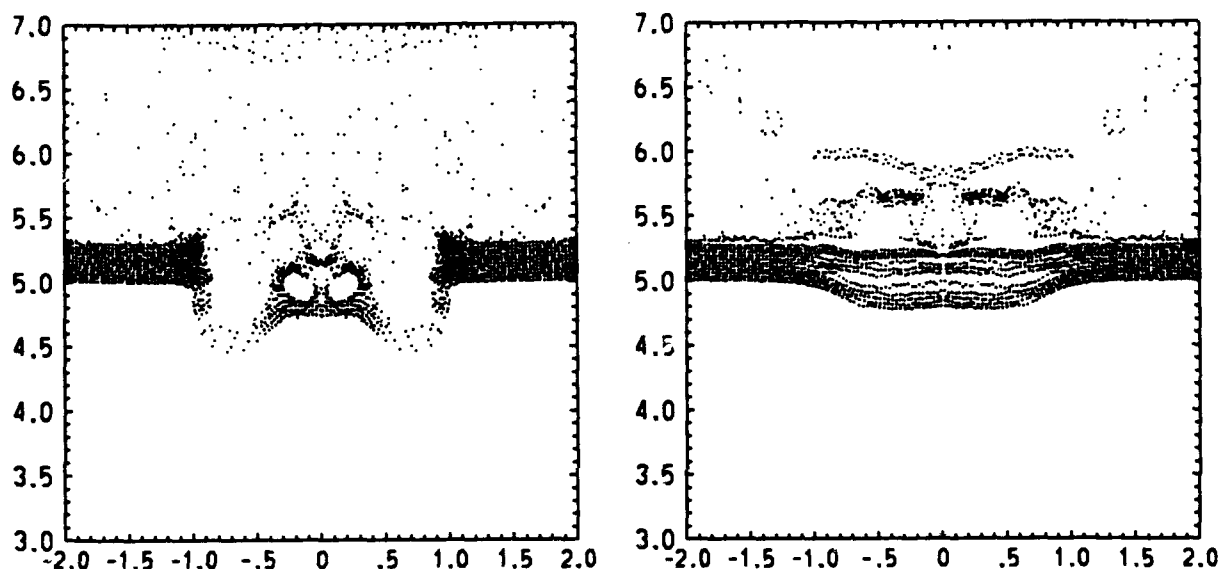
Figure 48. SPH material plots of WS-11 (left) and WS-12 (right) at 14 μs (disk).

The shear stress in the XY plane was plotted as a function of time for WS-11 and WS-12 calculations. These plots are presented in Figure 49. The plots demonstrate that the debris cloud hits the witness plate at 8.7 μs for WS-11 and 10.1 μs for WS-12. In this figure, the negative peak shear stress was greater in magnitude for WS-12. The data plotted past 14 μs is reflecting the numerical problems described above.

Material plots of the WS-12 calculation corresponding to photographic times (Fig. 25) are shown in Figure 50. The SPH debris cloud expanded in the axial direction at a similar speed to the experimental debris cloud for the WS-12 test. Radial expansion was somewhat slower than what is seen in the experiment. The experimental cloud was calculated to have respective axial and radial velocities o 14.1 and 7.3 km/s. The SPH debris cloud produced by a flyer plate had a leading edge velocity of 11.2 km/s and a radial velocity of about 3.8 km/s for WS-12. The

experimental cloud hit the witness plate at about 8 μs. The SPH cloud impacted the witness plate
at 10.1 μs. The SPH calculation predicts less damage to the WS-12 witness plate up to 14 μs
than what is revealed in the experiment. Experiment shows definite rupture of the witness plate
by 13 μs. Figure 48 (right) shows calculation of WS-12 at 14 μs.

Cloud and ejecta divergence angles converged to values of 52 and 50 deg, respectively, for the
WS-12 calculation.
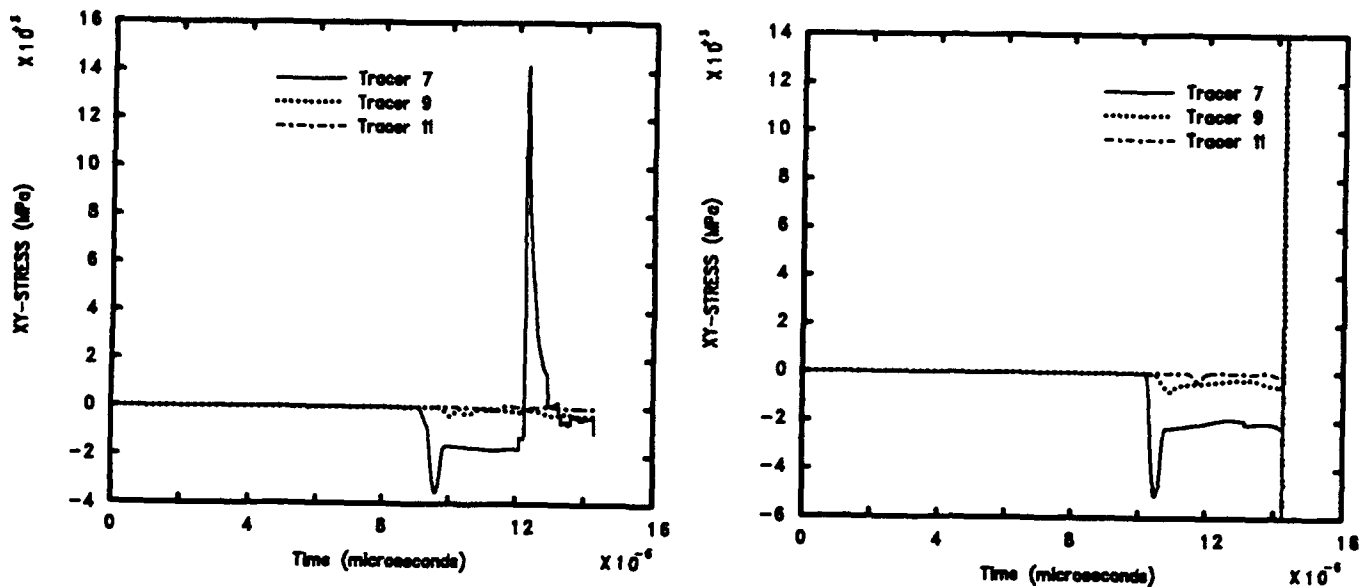
Figure 49. SPH xy stress plots of WS-11 and WS-12 (disk).
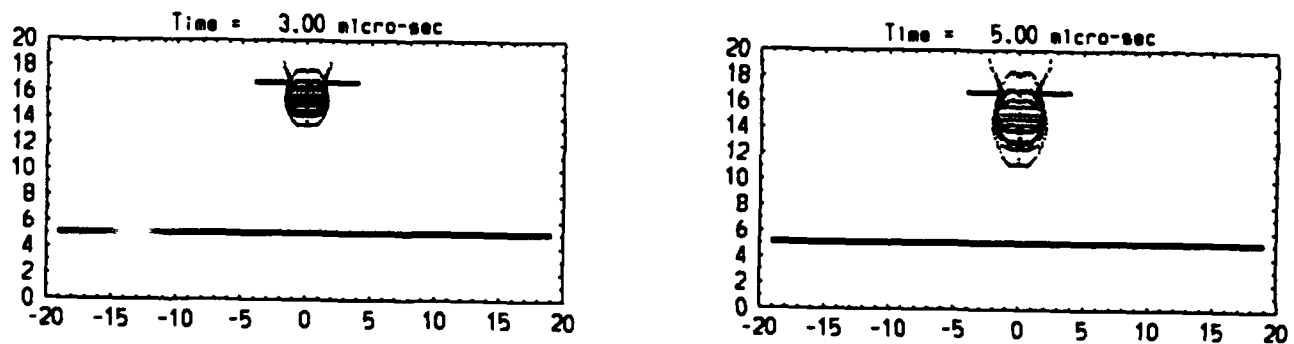
Figure 50. SPH material plots corresponding to WS-12 side view photograph times (disk).

52

6.3.6 Comparison of CTH and SPH Results

Several comparisons can be made between the CTH and SPH calculations of the WS-11 and WS-12 experiments. Areas of comparison include stand-off shield hole size, witness plate impact time, debris cloud dynamics, and damage to the witness plate. These values are summarized in Table 7.

For WS-11, stand-off shield hole size is compared between SPH and CTH since this value could not be obtained from the experiment. The SPH code predicted slightly larger (5%) stand-off shield hole size for both the disk-shaped and spherical projectiles. The values of hole size for the WS-11 calculations are listed in Table 7. The empirical model predicted a hole size of 1.56 cm for the WS-11 calculation.

Table 6 summarizes the average radial and axial velocities for WS-11 and WS-12 experiments and calculation. The axial and radial velocities of the CTH and SPH calculations were similar to each other for both spherical and plate projectiles. The debris cloud calculated by SPH using flyer plates more closely resembles the axial and radial velocities of the debris cloud produced by the experiment. The SPH calculation was about 11 percent closer to the experimental axial velocity and 13 percent closer to the experimental radial velocity than CTH. Both codes predicted that WS-12 would have a lower axial velocity than WS-11 (for disk-shaped projectiles). This is contrary to experimental results. The WS-12 experiment resulted in a faster axial velocity than what was seen in WS-11.

Damage to the witness plate was better matched to the experiment by both CTH and SPH using spherical projectiles. Like the experiment, perforation was predicted to occur sooner in the witness plate of WS-12 than that of WS-11 when using spherical projectiles. The opposite was found using disk-shaped projectiles. The CTH calculation predicted perforation to occur at about 23 μs for WS-12 and 21 μs for WS-11.

For WS-12, the diameter of the stand-off hole produced by a spherical projectile was closer to the results of the empirical model (1.75 cm) than the diameter predicted by CTH. The values of stand-off shield hole diameter are listed in Table 7.

The results of the CTH and SPH calculation using a spherical projectile matched the experiment better for witness plate damage than the results using a disk-shaped projectile. A closeup of the

53

Table 7. Characteristics of experiments and calculations, WS-11 and WS-12.

	WS-11			WS-12		
	CTH Sphere/Disk	SPH Sphere/Disk	Experiment	CTH Sphere/Disk	SPH Sphere/Disk	Experiment
Stand-off Shield Hole Size (cm)						
at 10 μs	1.4/1.9	1.5/2.0	a	1.58/2.5	1.74/2.7	a
at 17 μs	1.4/1.9	1.7/b	a	1.6/2.5	1.82/b	a
at 20 μs	1.4/1.9	1.8/b	a	1.6/2.5	1.86/b	a
at 30 μs	b	1.9/b	a	b	1.98/b	a
at 60 μs	b	1.9/b	a	b	2.04/b	a
Witness Plate Impact Time (μs)	11.5/10.3	11.2/9.1	8.7	11.75/11.2	11.4/10.1	8.0
Debris Cloud Dynamics						
Length, l (cm)				Length, l (cm)		
at 5 μs	4.7/5.6	5.0/6.2	6 .6	4.57/5.09	5.0/5.6	7.0
at 10 μs	9.5/11.28	10.2/hit plate	Hit Plate	9.52/10.24	10.1/11.4	Hit Plate
Width, w (cm)				Width, w (cm)		
at 5 μs	3.7/5.0	4.5/4.0	5.5	3.8/4.0	4.5/4.3	9.0
at 10 μs	7.1/6.4	8.2/6.6	Hit Plate	7.16/6.13	8.8/6.6	Hit Plate
Late Time Divergence Angles (deg)				Late Time Divergence Angles (deg)		
Cloud	80/12	78/66	a	80/12	80/52	a
Ejecta	c	74/54	a	c	76/50	a
Witness Plate Damage						
Peak y-Velocity (m/s)				Peak y-Velocity (m/s)		
at 16 μs	95^e/1400^e	650^d/b	a	227^e/1102^e	1110^d/b	a
at 60 μs	b	491^d/b	a	b	743^d/b	a
Peak y-Displacement (cm)				Peak y-Displacement (cm)		
at 16 μs	0.018^e/0.473^e	0.059^d/b	a	0.043^e/0.37^e	0.559^d/b	a
at 60 μs	b	2.650^d/b	a	b	6.2^d/b	a

[a] Experimental pulsed laser photo did not provide this data.
[b] Calculation terminated prior to this time.
[c] Mesh boundary did not extend to include ejecta
[d] Value at Tracer 7
[e] Value at Tracer 9

witness plate at the area of impact is shown in Figures 30 and 43. Figure 30 is the results from CTH using a spherical projectile. Figure 43 is results for a spherical projectile. These figures show that perforation has occurred in the witness plate of WS-12 while that of WS-11 is only bulging at the back surface. Similar results were seen in the experiment. Figures 36 and 48 are the CTH and SPH results using a disk-shaped projectile. For both CTH and SPH, perforation first occurs in the witness plate of WS-11.

7.0 CONCLUSIONS

This report has described the numerical simulations of five HV impact experiments that were performed by SNL. Each of the five experiments with the exception of HOLO17 used flyer plate projectiles. The HOLO17 experiment used a spherical projectile.

The numerical simulations were carried out independently using two different hydrocodes: CTH and SPH. The simulations of XH-9 and XH-10 were run with an equivalent mass sphere. WS-11 and WS-12 were simulated with both spherical and disk shaped projectiles. The simulations detailed in this report have accomplished the following objectives:

- precise dynamic characteristics at specific Lagrangian tracer points and qualitative graphical results have provided a better understanding of the complex phenomena that occur when HV projectiles impact and penetrate thin target layers and form debris clouds.

- we have applied a state of the art experimental data base to be simulated using two sophisticated hydrocodes. This has allowed for the benchmarking and validation of these codes.

- the modeling techniques described in this report serve to extend the ability to use both experimental and theoretical tools for the analysis of HV impact.

- the results of these simulations have helped to describe the discrepancies between experimental and numerical simulations. This will allow code developers to identify areas of the numerical theory that require improvement.

The CTH and SPH codes generally predicted similar results when modeling the five HV impact experiments. With the exception of the XH-9 and XH-10 calculations, the predictions of one code for hole size, debris cloud dynamics, witness plate impact time, and plate deformation were mostly within 10 percent of the other.

The calculations in which both spherical and disk-shaped projectiles were used gave evidence of the large effect that projectile geometry has on the characteristics and damage potential of the debris cloud. The result of experiments XH-9 and XH-10 show that slight yaw angles and orientations of similar disk-shaped projectiles greatly influences the characteristics of the debris cloud. Further investigation is necessary to determine the differences in damage potential

55

produced by differences in projectile geometry and orientation given that all other parameters are equal.

Qualitatively, the codes modeled the physical processes of these impacts very well. In all cases the response of the projectile stand-off shield and witness plates qualitatively resembled experimental results. The simulations of WS-11 and WS-12 using disk-shaped projectiles did not match experimental results for damage (i.e., extent of penetration) up to 21 μs. Unlike the experimental results, the witness plate in WS-11 was perforated before the one in WS-12. Experimental results show no perforation to the witness plate in WS-11 up to 60 μs. This disagreement may be due to the fact the preflight irregularities were not modeled in the calculations. Also, the plates in the calculations were perfectly flat with respect to the stand-off shield. The projectile in WS-12 was about the same thickness as the one in WS-11 but its diameter was 51 percent larger. This had the effect of dispersing its kinetic energy over a wider area on the stand-off plate as well as the witness plate. For this reason, the damage potential of the increased amount of kinetic energy in WS-12 was offset by its larger diameter.

When modeling the WS-11 and WS-12 experiments using spherical projectiles instead of a flyer plate, the predominate difference was projectile kinetic energy (there was a difference in radii of the projectiles but this did not seem to affect the debris cloud characteristics as much). In these cases, both codes showed that this difference manifested itself in an increased level of damage to the witness plate for WS-12. It is questionable whether it is legitimate to compare calculations using spherical projectiles with experiments using flyer plates. However, results for the WS-11 and WS-12 calculations using spherical projectiles correctly predicted the survival status of the witness plate. The WS-11 experiment showed no penetration of the witness plate up to 60 μs while the WS-12 experiment showed failure occurring at 13 μs. The SPH calculations agreed with this result. The CTH calculations of these experiments showed no perforation in either calculation up to 17 μs. However, the damage was considerably more extensive for the WS-12 calculation at this time.

For those areas in which a quantitative measure was available (e.g., debris cloud parameters), the codes best matched the experimental results for axial velocities of the debris clouds. A summary of the quantitative differences associated with the code and the experimental results are found in Table 8. Negative quantities indicate under-predictions, positive values indicate overpredictions. Percentage differences in the measured quantities between SPH and CTH are listed in Table 9.

Table 8. Relative difference between code and measurable experimental results.

	HOLO17		XH-9		XH-10		WS-11 Sphere/Plate		WS-12 Sphere/Plate	
	CTH	SPH	CTH	SPH	CTH	SPH	CTH	SPH	CTH	SPH
Hole size, experiment, %	-47	-41	a	a	a	a	a	a	a	a
Hole size, empirical, %	3.6	15	-35	-25	-18	-23	-10/a	22/a	-9/a	17/a
Axial velocity, %	-21	-14	24	9	-22	-32	-27/-14	-22/-5	-31/-28	-28/-21
Radial velocity, %	-22	28	24	-11	-25	-47	-49/-54	-41/-51	-40/-52	-40/-48
Impact time, %	a	a	20	39	a	-47	32/18	29/5	47/40	43/26

[a] Calculation was terminated, did not apply in this case or could not be retrieved from experimental data.

Table 9. Percent difference in calculated quantities between CTH and SPH.

	HOLO17	XH-9	XH-10	WS-11 Sphere/Plate	WS-12 Sphere/Plate
Hole size, %	10	13	8	29/5	16/4
Axial velocity, %	7	13	15	7/11	4/10
Radial velocity, %	13	39	42	14/6	0.0/9
Impact time, %	a	14	a	3/12	3/10

[a] Value did not apply in this case or calculation was terminated.

There was a considerable difference in the computational requirements of the codes. All SPH calculations were easily run on a 64 Mb workstation, while the fine-meshed CTH calculations required the use of the Phillips Laboratory Cray2 unless the computational space was judiciously reduced in size without changing the cell size.

8.0 RECOMMENDATIONS

The experimental results of XH-9 and XH-10 and the numerical results of modeling spherical versus flat projectiles demonstrate the importance of projectile geometry on the damage profile of the secondary plate. Although XH-9 and XH-10 were designed to be as identical as possible, small differences in projectile shape and orientation affected the shape of the debris cloud considerably. The numerical simulations of WS-11 and WS-12 also indicate the importance of projectile geometry. Spherical and disk-shaped projectiles used in these simulations were equivalent in mass and initial kinetic energy but produced different results. Additional calculations should be run using projectiles with small differences, i.e., yawed versus flat on impacts. This could be accomplished to an extent in two dimensions but may require the use of three-dimensional calculations.

A second area of interest affecting the numerical prediction of HV impacts is the application of fracture models. Experimental results in the form of photographs and posttest fragments can be used to assess the degree of fragmentation of an impact scenario. Experimental photographs that are clear, showing fragment size and distribution, can then be compared to numerical calculations involving various fracture models.

Further analysis of the simulated debris clouds to retrieve material phase information would be useful and may be comparable to experimental results. Limited material phase information can be retrieved from experimental results by examining the surface roughness of captured fragments to deduce which phases the material has experienced. Also, the characteristics of the surface of the postimpact witness plate may reveal the phases characteristics of the debris cloud. The mass of the fragments found after the impact can be compared to the initial mass of the objects involved in the impact. Differences may point to the amount of mass vaporized during the impact. Hydrocodes incorporating sophisticated equation-of-state algorithms can be used to classify the mass in a given calculated debris cloud into one of the three states of matter based on density and temperature.

REFERENCES

1. Holland, P. M. *et. al.*, "Hydrocode Results for the Penetration of Continuous, Segmented and Hybrid Rods Compared with Ballistic Experiments," <u>Int. J. Impact Engineering</u>, Vol 10, Nos. 1-4, pp. 241-250, 1990.

2. Holin, K. S., "Hydrodynamics Code Calculations of Debris Clouds Produced by Ball-Plate Impacts," <u>Int. J. Impact Engineering</u>, Vol. 10, Nos. 1-4, pp. 231-239, 1990.

3. Brewer, E. D. *et. al.*, <u>Shield Design, Analysis, and Testing to Survive Stainless Steel Projectiles</u>, TM-11381, Oak Ridge National Laboratory, Oak Ridge, TN, January 1990.

4. Chhabildas, L. C. *et. al.*, "Hypervelocity Impact Tests and Simulations of Single Whipple Bumper Shield Concepts at 10 km/s," <u>Int. J. Impact Engineering</u>, Vol. 14, 1993.

5. McGlaun, J. M. *et. al.* , <u>CTH User's Manual and Input Instructions</u>, Sandia National Laboratories, Version 1.020, Albuquerque, NM, July 90.

6. Libersky, L. D. and Petschek, A.G., <u>Smooth Particle Hydrodynamics With Strength of Materials</u>, CETR, New Mexico Institute of Mining and Technology, Socorro, NM.

7. Petschek, A. G. and Libersky, L. D., <u>Cylindrical Smoothed Particle Hydrodynamics</u>, CETR, New Mexico Institute of Mining and Technology, Socorro, NM , 1992.

8. Kinslow Ray, ed., <u>High-Velocity Impact Phenomena</u>, Academic Press, New York, 1970.

9. Chhabildas, L. C. *et. al.*, "Spall Strength Measurements on Shock-Loaded Refractory Metals," <u>Shock Compression of Condensed Matter</u> , (S. C. Schmidt *et al.*, eds.) pp. 429-432, Elsevier Science Publishers, B.V., Amsterdam., 1989.

10. Hertel, E. S. *et. al.*, "Whipple Bumber Shield Simulation," <u>Shock Compression of Condensed Matter</u>, (S. C. Schmidt *et al.*, eds.) pp. 987-990, Elsevier Science Publishers, B.V., Amsterdam, 1991.

11. Chhabildas, L. C., *et. al.*, "Whipple Bumper Shield Tests at over 10 km/s," <u>Shock Compression of Condensed Matter</u>, (S. C. Schmidt *et al.*, eds.) pp, 991-994, Elsevier Science Publishers, B.V., Amsterdam, 1991.